Sodium-chromium covariation in residual clinopyroxenes from abyssal peridotites sampled in the 43°–46°E region of the Southwest Indian Ridge / Seyler, Monique; Brunelli, Daniele. - In: LITHOS. - ISSN 0024-4937. - 302-303:(2018), pp. 142-157. [10.1016/j.lithos.2017.12.018]

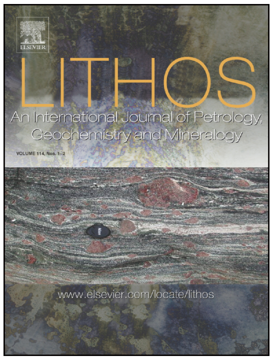

Sodium-chromium covariation in residual clinopyroxenes from abyssal peridotites sampled in the 43–46°E region of the Southwest Indian Ridge

Monique Seyler, Daniele Brunelli

PII: S0024-4937(17)30453-X
DOI: https://doi.org/10.1016/j.lithos.2017.12.018
Reference: LITHOS 4517

To appear in:

Received date: 29 May 2017
Accepted date: 20 December 2017

Please cite this article as: Monique Seyler, Daniele Brunelli , Sodium-chromium covariation in residual clinopyroxenes from abyssal peridotites sampled in the 43–46°E region of the Southwest Indian Ridge. The address for the corresponding author was captured as affiliation for all authors. Please check if appropriate. Lithos(2017), https://doi.org/10.1016/j.lithos.2017.12.018

Sodium-chromium covariation in residual clinopyroxenes from abyssal peridotites sampled in the 43–46°E region of the Southwest Indian Ridge

Monique Seyler[a,*] and Daniele Brunelli[b,c]

[a] Univ. Lille, CNRS, Univ. Littoral Côte d'Opale, UMR 8187, LOG, Laboratoire d'Océanologie et de Géosciences, F 59000 Lille, France. E-mail: monique.seyler@univ-lille1.fr

[b] Dipartimento di Scienze Chimiche e Geologiche, Università di Modena e Reggio Emilia, via Campi, 103, 41125 Modena, Italy. E-mail: daniele.brunelli@unimore.it

[c] Istituto di Scienze Marine ISMAR-CNR, 40129 Bologna, Italy

* Corresponding author

ABSTRACT

Mantle-derived peridotites sampled at three dredge sites between the Discovery and Indomed fracture zones on the Southwest Indian Ridge axis are analyzed for petrography and major and trace element mineral compositions. While textures and microstructures are those typical of normal residual peridotites these rocks display a large compositional variation encompassing the whole spectrum of abyssal peridotites even at the scale of a single dredge site (≤ 1km). Particularly, clinopyroxenes in peridotites dredged at 44.03° E show a huge variation in sodium contents positively correlated with chromium concentrations. Observed Na-Cr enrichments exceed the commonly reported contents of the spinel abyssal peridotites. Similar values are only found in very few peridotite samples collected at ultra-slow spreading ridges. Major substitutions governing the compositions of these clinopyroxenes suggest that Na-Cr covariation is caused by a more rapid decrease in Al-Tschermak's molecule with respect to the sodic components jadeite ± kosmochlor, as Cr/Al increases and modal clinopyroxene decreases. We conclude that sodium and chromium enrichments must have occurred contemporaneously with aluminum depletion, i.e., during partial melting. Our modeling suggests that partial, non-modal, melting of a depleted peridotite in association with addition of sodium, by percolation of a Na-rich melt in the upwelling mantle, or Na diffusion from a nearby alkaline melt, may explain this enigmatic and counterintuitive trend.

Keywords

abyssal peridotite ; mid-oceanic ridge ; partial melting ; mantle metasomatism ; sodium-chromium correlation ; clinopyroxene

1. Introduction

Abyssal peridotites and Mid-Ocean Ridge Basalts (MORB) are considered as complementary, residual and magmatic, products resulting from adiabatic partial melting of the asthenospheric mantle beneath mid-ocean ridges. The increasing number of observations of natural samples, experiments and numerical modeling provide growing evidences for a lithologically non-uniform MORB mantle source (e.g., Hanson, 1977; Hirschmann and Stolper, 1996; Wood, 1979). Even those ridge sections not influenced by hot spot activity likely contain small amounts of mafic components such as eclogite or pyroxenite (e.g., Hirschmann and Stolper, 1996; Lambart et al., 2012, 2013;

Pertermann and Hirschmann, 2003). Isotopic compositional variability of abyssal peridotites does not systematically overlap with that of the associated basalts and extends to more depleted compositions in several localities (Cipriani et al., 2004; Harvey et al., 2006; Lassiter et al., 2014; Liu et al., 2008; Mallick et al., 2014, 2015; Salters and Dick, 2002; Stracke et al., 2011; Warren et al., 2009; Warren and Shirey, 2012). The idea of a low-solidus component with enriched isotopic signature in the MORB mantle source has been invoked to explain the lack of the most enriched isotopic compositions in residual peridotites with respect to associated MORBs (Salters and Dick, 2002; Liu et al., 2008; Mallick et al., 2014, 2015). As shown by petrological and numerical experiments, melting of a low-solidus component may considerably modify the melting process of the surrounding peridotite (Morgan, 2001; Katz and Weatherley, 2012; Lambart et al., 2016; Spiegelman and Kelemen, 2003; Weatherley and Katz, 2012). In addition, the small scale (< 1 km) modal and compositional variations created in the residual peridotite during melt extraction, segregation and transport processes, are significantly enhanced when melt-peridotite interaction is combined with a lithologically or mineralogically heterogeneous source (Brunelli et al., 2014; Lambart et al., 2012; Liang and Parmentier, 2010; Liang and Peng, 2010; Stracke and Bourdon, 2009). As a rule of thumb, residual compositions are more efficiently modified when greater is the compositional contrast (e.g., the degree of disequilibrium) between transient melts and partially molten peridotite. The largest variations are observed when alkaline or garnet equilibrated melts, possibly generated by melting of a low-solidus lithology, interact with a depleted peridotite equilibrated in the spinel stability field (Brunelli et al., 2014). Examples from a few geographic areas have demonstrated the ability of abyssal peridotites to record such chemically enriched melts, providing insight into source compositional heterogeneity (Brunelli and Seyler, 2010; Cipriani et al., 2009; D'Errico et al, 2016;

Hellebrand et al., 2002b; Mallick et al., 2015; Seyler et al., 2004, 2011; Warren et al., 2009).

In this study we present petrographic and chemical data of abyssal peridotites dredged in a section of the Southwest Indian Ridge (SWIR) whose basaltic crust is characterized by large isotopic and chemical variations. The peridotites sampled at the dredge 26 site during the SWIFT cruise (SWF-26) contain clinopyroxene showing enrichments both in sodium and chromium, up to very elevated concentrations, correlated with an increase in the apparent degree of melting. A review of global compositional variations in abyssal peridotites (Warren et al., 2016) reveals that similar depletion/enrichment trend is not unique but very rare, and found no satisfactory explanation. In an attempt to understand this enigmatic trend, we have characterized the major substitutions governing the evolution of the pyroxene compositions and modelled the Na and Cr compositions by combining partial melting and percolation of a Na-rich melt. Our results suggest possible relationships between the Na-Cr covariation and enriched, high-pressure melts, derived from a heterogeneous mantle source.

2. Geological setting

The SWIR is a major plate boundary separating Africa and Antarctica with an almost constant ultra-slow spreading rate of about 16 mm/yr (DeMets et al., 1990) from the Andrew Bain Fracture Zone (FZ) (32°E) to the Rodrigues triple junction (70°E). The basalts are normal and enriched MORB (N- and E-MORB), characterized by a large isotopic compositional diversity (Bezos et al., 2005; Chauvel and Blichert-Toft, 2001; Gautheron et al., 2015; Hamelin and Allègre, 1985; LeRoex et al., 1989; Mahoney et al., 1989; Meyzen et al., 2003, 2005), dominated by the DUPAL anomaly, whereas the peridotites dredged along-axis appear highly heterogeneous in modal, chemical and isotopic composition at all length-scales (Mallick et al., 2014, 2015; Seyler et al., 2003, 2004, 2011; Warren et al. 2009; Warren and Shimizu, 2010).

In the continuity of the systematic on-axis sampling of the 49-70°E region performed during the MD107 EDUL cruise (Mével, 1997), 31 other locations have been dredged along the neovolcanic zone between 30° and 50°E during the cruise MD121 SWIFT (South West Indian French Transit) operated by the R/V Marion Dufresne in 2001 (Humler et al., 2001). Only two on-axis dredge hauls (SWF-26 and SWF-27; Fig. 1) recovered mantle peridotites, both located in a non-transform discontinuity at 44°E, between the Discovery I (42.5°E) and the Indomed (46°E) FZs. In 2002, mantle peridotites were collected at a third dredge site (SC-08, 45.8°E) on the west side of the Indomed FZ near its intersection with the SWIR axis during the MD125 SWIFT bis–CARHOT cruise (Aslanian et al., 2002). The 43-46°E region is centered on a large positive residual geoid anomaly extending from 32°E to 55°E beneath the SWIR (LeRoex et al., 1989), at midway between the influence of the Marion (~38°E) and Crozet (~52°E) Islands, two hot spots presently located at ~250 km (Marion) and ~1000 km (Crozet) south of the ridge axis (Müller et al., 1993). No peridotite but few basalt compositions from four dredge sites (Fig. 1), including a glass retrieved with the SWF-26 peridotites, have been published for the region of interest. Their compositions vary from N-MORB in the 43°–44° E segment to E-MORB and alkali-basalt close to the Indomed FZ (Hamelin and Allègre, 1985; LeRoex et al., 1989; Mahoney et al., 1989). In the 32°–47° E region isotopic compositions are typical of the regional Indian ocean mantle (Chauvel and Blichert-Toft, 2001; Hamelin and Allègre, 1985; Mahoney et al., 1989), which might locally contain fragments of lower continental crust (Gautheron et al., 2015).

3. Sample selection and petrography

Dredges SWF-26, SWF-27 and SC-08 each recovered about 150-160 kg of strongly serpentinized and weathered peridotites occurring as rounded blocks of ~15–30 cm in diameter. Rare dunites and ~40 kg of altered basalt were also recovered in dredge SWF-26, while dredge SC-08 included olivine-plagioclase-phyric basalts. Glassy fragments were present in all the three dredges but gabbroic and pyroxenitic materials were lacking. Visual inspection on hand samples shows that dredges SWF-26 and SC-08 are dominated by spinel-lherzolites while dredge SWF-27 contains spinel-harzburgites. Three lherzolites (SWF-26-2-5, SWF-26-2-9, SWF-26-2-11 containing 5–11% modal clinopyroxene, Table 1) and three harzburgites (SWF-26-2-7, SWF-27-1-12, SC-08-03 2–3% modal clinopyroxene, Table 1) have been selected for this study. Samples are 60–80% serpentinized, but primary minerals of all phases have been preserved except in SWF-27-1-12 and SC-08-03 where olivine is fully replaced by serpentine. Selected samples have coarse-granular texture, with a weak high-temperature foliation (Supplementary Data Fig. S1A–B). They lack evidence for magmatic veins and plagioclase impregnation or its alteration products; in addition, as shown below, their spinel has very low-Ti content. Based on these criteria, selected samples are inferred to be residual (Dick and Bullen 1984; Seyler and Bonatti, 1997). Reconstructed primary modes plot within the SWIR abyssal peridotite field (Table 1; Fig. 2).

In thin section samples display near-similar textural features. Olivine granular assemblages of ~10-20 mm in diameter are made of 0.2-0.5 mm sized, subhedral grains with curvilinear boundaries. Orthopyroxenes and clinopyroxenes are commonly associated in bi- (orthopyroxene + clinopyroxene) or mono-mineralic (orthopyroxene or clinopyroxene) aggregates (Fig. 3). In the lherzolites SWF-26-2-9, SWF-26-2-11 and the harzburgite SC-08-03, the orthopyroxene assemblages are not elongated and of the same size as olivine, coexisting with smaller-sized (<1 mm) clinopyroxene. In contrast, the lherzolite SWF-26-2-5 contains smaller orthopyroxene crystals but abundant , up to 15 mm, elongated aggregates of clinopyroxenes defining a foliation (Fig. 3A). In all samples pyroxene aggregates are characterized by jagged, strongly irregular outlines with deep olivine-filled embayments (Fig. 3B; Supplementary Data Fig. S2A–C). Within the aggregates, pyroxene crystals are randomly oriented, with contact boundaries varying from straight (Fig. 3D) through curvilinear (Fig. 3E) to interlocking (Fig. 3F). Orthopyroxene blebs are commonly present along clinopyroxene-clinopyroxene contacts (Fig. 3E,F). Both pyroxene types show thin exsolution lamellae of the complementary phase. Spinel generally grows along the tips of elongated clinopyroxene crystals or forms arrays of discrete grains defining alignments parallel to the foliation (Supplementary Data Fig. S2B,C). In addition, both mineral phases display tiny extensions that propagate into the rock volume among the adjacent olivine grains and along olivine-orthopyroxene contacts (Supplementary Data Fig. S2B,D,E); this interstitial material occasionally ends as thin films or micro-cracks crossing through the adjacent crystals (Supplementary Data Fig. S2F). Similar propagation textures, but involving clinopyroxene and plagioclase, also occur in oceanic gabbros (e.g., Agar and Loyd, 1997; Dick et al., 2002); they have been reproduced experimentally and explained as the result of a partial melting reaction triggered by water-rich fluids, that starts on the primocryst boundaries and proceeds by dissolution/precipitation of the primocrysts (Koepke et al., 2005). In abyssal peridotites, orthopyroxene - olivine textural relationships are generally interpreted as resulting from pyroxenes incongruent melting in the upwelling melting mantle (Ceuleneer et al.,1988; Nicolas,1986). Similar textures also develop where melts, generated at deeper levels, migrate upward and react with residual peridotites (Daines and Kohlstedt, 1994; Kelemen et al., 1992; Seyler et al., 2007), leading to pyroxene dissolution and olivine precipitation (Kelemen et al., 1992). Based on this interpretation and on Koepke et al. (2005)' work, we suggest that extreme resorption and propagation textures in clinopyroxene and spinel of abyssal peridotites also form by partial melting and/or melt-rock reactions during the final stage of melting. Alternatively, thin clinopyroxene and spinel material, interstitial or filling cracks, may represent frozen melts injected into fine-scale porosity structure, as observed in some primitive cumulates (Natland and Dick, 2001) or in a partially molten rock still in deformation (Seyler et al., 2001 and references therein). It is noteworthy that intergranular extensions of coarse clinopyroxenes are often interconnected, with preferential crystallization of clinopyroxene + spinel intergrowths at the junctions, suggesting interconnection of a former intergranular melt over cm-scale distances (Seyler et al., 2003). Plastic deformation and dynamic recrystallization are restricted in intensity and space, affecting preferentially the borders of the pyroxene crystals or aggregates. These grains appear twisted or broken (Fig. 3D); the rare recrystallized grains are anhedral, with occasional 120° triple junctions and lack of exsolutions. Spinel intergrowths with pyroxene neoblasts are locally observed where spinel arrays merge with the recrystallized borders.

In conclusion the studied peridotites display textures similar to those considered as residual upper mantle following melt extraction (e.g. Ceuleneer and Cannat, 1997; Dick et al., 2010; Seyler et al., 2007). Crystal deformation is limited probably because intergranular melt reacted with the peridotite during equilibration at high temperature in the asthenosphere - lithosphere boundary layer (Dick et al., 2010). Clinopyroxene and spinel are commonly associated in similar microstructures and appear to be the last phases to have been mobilized before freezing. There is no evidence for modal metasomatism, i.e., the orthopyroxene phase contains no mineral inclusions such as those described in some peridotites (Luguet et al., 2003; Seyler et al., 2004), magmatic sulfides are lacking and late-stage crystallization from trapped melts is modest compared to some abyssal peridotites (Seyler et al., 2001, 2007; Suhr et al., 2008).

4. Mineral compositions

4.1. Analytical methods

Olivine, pyroxenes and spinel major elements were analyzed using the automated CAMECA-CAMEBAX electron microprobe of the CAMPARIS micro-analysis center (University of Paris 6). The accelerating voltage was 15 kV and beam current was 40 nA (15 nA for Na). A 2 μm beam size was used for all minerals, except a subset of pyroxenes, for which average core compositions including exsolution lamellae were obtained with a defocused beam (10–15 μm). Detection limits are within 0.01–0.03 wt.%. Pyroxene trace element abundances were determined at the university of Montpellier 2, both by secondary ion microprobe spectrometry (SIMS) with the Cameca IMS5f and by inductively coupled plasma-mass spectrometry (ICP-MS) coupled with laser ablation (LA). The LA system is an automated platform Microlas (Geolas Q+) equipped with a 193 nm laser Excimer CompEx 102 from LambdaPhysik. The measurements were analyzed on a ThermoFinnigan Element 2 High Resolution ICP-MS using a single collector double-focusing field Element XR (eXtended Range) with a sensitivity of ca. 1 billion cps/ppm on ^{115}In. The reader is referred to Seyler et al. (2003, 2011) for a complete description of the analytical methods. Four samples from dredge SWF-26, one sample from dredge

SWF-27 and one sample from dredge SC-08 were analyzed for mineral major elements. Trace elements were acquired on clinopyroxenes and orthopyroxenes of SWF-26-2-5, SWF-26-2-7 and SWF-26-2-9, while only clinopyroxenes of SWF-26-2-11 were analyzed. Clinopyroxenes were analyzed in core and rim and for different textural types with a beam size of 25 μm (SIMS) and 100 μm (LA-ICPMS). Orthopyroxenes were analyzed in core only, with a beam size of 25 μm (SIMS) and 120 μm (LA-ICPMS). Mineral major and trace element data are presented in Tables 2 and 3; because LA-ICP-MS and ion probe concentrations are within analytical errors (see Seyler et al., 2011 for a comparative study of the results obtained with the two techniques), all measurements have been averaged for each sample in Table 3. Complete trace element data of orthopyroxenes and clinopyroxenes are available in Supplementary Data Table S1.

4.2. Major element compositions

Olivine forsterite contents in samples SWF-26-2-5, SWF-26-2-7, SWF-26-2-9 and SWF26-2-11 average 90.0, 90.8, 90.4 and 90.2, respectively, with standard deviation <0.2 wt.% in individual samples. Average NiO content is 0.38 ± 0.04 wt.% for the four samples. In the other three samples olivine was not analyzed because fully altered.

Enstatitic and diopsidic pyroxenes show a compositional range nearly encompassing the whole SWIR compositional field (Fig. 4). Al_2O_3 and Cr_2O_3 concentrations are positively correlated in individual samples, both decreasing with decreasing grain size and from core to rim (Fig. 4A, B), a characteristic of mantle peridotites ascribed to subsolidus re-equilibration at high temperature. During this process Cr# [= 100. Cr / (Cr + Al)] slightly decreases in orthopyroxene (Fig. 4C) and remains stable in clinopyroxene (Fig. 4D). In contrast, Cr_2O_3 and Cr# in core compositions are negatively correlated with Al_2O_3 from sample to sample, as expected in a set of residual peridotites that experienced variable degree of melt depletion. The clinopyroxene-rich lherzolite SWF-26-2-5 has orthopyroxenes with high Al_2O_3 contents (5.4 ± 0.2 wt.%), while Al_2O_3 in its clinopyroxenes range from ~7.5 to ~4.0 wt.%, averaging 6.7 ± 0.5 wt.% in the core of the coarser (≥ 0.5 mm) grains. In this sample, both pyroxenes have low Cr_2O_3 contents (0.5 ± 0.1 wt.% in orthopyroxene; 0.8 ± 0.1 wt.% in clinopyroxene). At the opposite end, pyroxenes of the harzburgite SWF-26-2-7 have the lowest Al_2O_3 contents (< 3 wt.% in orthopyroxene; < 4.5 wt.% in clinopyroxene) and the highest Cr_2O_3 contents (1.8 ± 0.1 wt.% in clinopyroxene). The pyroxene compositions of the other lherzolites average 5.0 ± 0.3 wt% in orthopyroxene and 6.2 ± 0.5 wt.% in clinopyroxene, while the pyroxenes of the harzburgites SWF-27-1-12 and SC-08-03 are moderately depleted in Al_2O_3 (4.0 ± 0.4 and 4.9 ± 0.2 wt.%, respectively in orthopyroxene; 5.1 ± 0.1 and 5.7 ± 0.4 wt.%, respectively, in clinopyroxene). Cr_2O_3 in clinopyroxenes are also within the range of average abyssal peridotites, with 1.2 ± 0.1 wt.% in the lherzolites and 1.4–1.5 ± 0.1 wt.% in the harzburgites. Pyroxenes Mg# [= 100.Mg / (Mg + Fe^t)] are poorly correlated with Al_2O_3 (Fig. 4E, F); in particular, SC-08-03 clinopyroxenes have high Mg# and SWF-26-2-7 clinopyroxenes have low Mg# with respect to the Al_2O_3 content. Nevertheless, except for SC-08-03, Mg# in ortho- and clinopyroxenes are nearly similar to Mg# in coexisting olivine (K_D ~1). Application of two-pyroxene thermometer of Brey and Köhler (1990) leads to equilibrium temperatures between 1016° and 1053°C at 1.2 GPa for all samples, except a slightly lower temperature (943°C) for SWF-26-2-5, indicating that the compositions measured in the pyroxene cores represent subsolidus compositions.

Na_2O and TiO_2 in clinopyroxenes are highly variable in the whole sample set, but do not vary within individual samples (Fig. 5). Clinopyroxene Na_2O concentrations are very low in the harzburgite SWF-27-1-12 (0.15 wt.%), increase in SWF-26-2-5 (0.43 ± 0.04 wt.%) to reach 0.70–0.75 wt.% in SWF-26-2-9, SWF-26-2-11 and SC08-03.

Clinopyroxenes of the harzburgite SWF-26-27 are anomalously enriched in Na_2O (1.43 ± 0.08 wt.%). At the scale of the sample set there are no obvious correlations between Na_2O and Al_2O_3 (Fig. 5A); however, the four samples from the dredge SWF-26 show a clear positive correlation in the Na_2O–Cr_2O_3 diagram (Fig. 5B). On the whole, TiO_2 concentrations in clinopyroxenes are quite low in all samples (< 0.15 wt.%) with the exception of SWF-26-2-9 (~0.22 wt%) that still plots below the main trend of the SWIR rocks (Fig. 5C). There is no correlation between Na_2O and TiO_2 (Fig. 5C).

Spinel compositions also vary widely from sample to sample (Fig. 6). In dredge SWF-26 compositions encompass the full range of abyssal peridotite spinels, with Cr# varying from ~12 in the clinopyroxene-rich lherzolite SWF-26-2-5, through ~18–19 in the lherzolites SWF-26-2-9 and SWF-26-2-11 to ~47 in the harzburgite SWF-26-2-7. Mg# is negatively correlated, ranging from ~79 in the clinopyroxene-rich lherzolite SWF-26-2-5, through ~75 in the other two SWF-26 lherzolites to 61 in the harzburgite SWF-26-2-7. Spinel Cr# in the other harzburgites are significantly lower than in SWF-26-2-7 (SC-08-03: Cr# 23, Mg# 74; SWF-27-1-12: Cr# 30, Mg# 68). All analyzed spinels have TiO_2 contents ≤ 0.1 wt%, indicating that they are not (re)equilibrated with plagioclase or affected by late-stage interaction with a magma.

Averaged Cr# in coexisting orthopyroxene, clinopyroxene and spinel are well correlated in the studied sample set, with K_D within the usual range of abyssal peridotites (Dick and Bullen, 1984). Mineral Cr# is a function of whole rock Cr#, which reflects the degree of depletion in magmatic components and thus widely used as a proxy for the extent of partial melting in residual mantle peridotites (Hellebrand et al., 2001). Fig. 7 shows that spinel Cr# in the studied samples increases with increasing modal olivine and decreasing modal clinopyroxene as expected for residues of increasing degrees of melt depletion by partial melting. It also appears that the correlation between the modes and the spinel Cr# is not linear, the latter increases more significantly as the rocks become more refractory. Using the relation between spinel Cr# and extent of partial melting established by Hellebrand et al. (2001), SWF-26 peridotites appear to have undergone varying amounts of melt extraction, corresponding to ~3% for the clinopyroxene-rich lherzolite, ~7% in the lherzolites SWF-26-2-9 and SWF-26-2-11 and ~16% in the harzburgite SWF-26-2-7. Samples SWF-27-1-12 and SC-08-03 would have experienced ~12% and ~9% melting, respectively. These results do not take in account possible degrees of melting in the garnet stability field (Hellebrand et al., 2001).

4.3. Compositional variations of clinopyroxenes of dredge SWF-26 peridotites

Clinopyroxenes of the four SWF-26 samples define a positive trend in the Cr_2O_3 -Na_2O diagram (Fig. 5B), with the clinopyroxene-rich lherzolite SWF-26-2-5 at the lowest Na_2O contents and the harzburgite SWF-26-2-7 at the highest values. Such a feature is inconsistent with the opposite Cr and Na behaviour resulting from magmatic processes. In addition, the high enrichments both in Cr_2O_3 (1.3–1.6 wt%) and Na_2O (1.5–2.1 wt%) observed in SWF-26-2-7 clinopyroxenes are clearly in excess with respect to the concentrations commonly measured in clinopyroxenes of abyssal peridotites. Similar unusual clinopyroxene compositions have only been recognized in a few dredges from ultra-slow spreading ridges in the SWIR (Seyler et al., 2003, 2011) and Arctic ocean (D'Errico et al., 2016; Hellebrand et al., 2005; Hellebrand and Snow, 2003; Lassiter et al., 2014).

Fig. 8 shows the variations of the major element compositions (in numbers of atoms per formula unit) of clinopyroxenes from the dredges containing clinopyroxenes significantly enriched in Na_2O and Cr_2O_3 from the Arctic and Southwest Indian ridges, hereafter referred as 'NaCr' dredges. They are compared with the global dataset of residual abyssal peridotites from Warren (2016)'s compilation. Although originated from different localities, all clinopyroxenes from 'NaCr' dredges define relatively well constrained linear trends, clearly distinct from the global dataset. With progressive depletion in Al, the 'NaCr' dredge samples have progressively higher Si resulting in a steeper slope with respect to the residual abyssal peridotite field (Fig. 8A); clinopyroxenes of 'NaCr' dredges also distinguish by a slightly lower Fe + Mg trend (Fig. 8B) and a clear decreasing Ca trend (Fig. 8C). In spite of the large compositional scatter global trends clearly show conjugate depletion in Na and Al (Fig. 8E) or Na and Al^{VI} (Fig. 8F). The curvature of the trends reflects the higher incompatibility of Na relative to Al during partial melting. In contrast samples from the 'NaCr' dredges show a negative Na-Al trend and no correlation between Na and Al^{VI}. In all sample sets, both Al^{IV} and Al^{VI} decrease with decreasing Al, but in the 'NaCr' dredges, Al^{IV} decreases faster (Fig. 8G) and Al^{VI} decreases slower (Fig. 8H). A consequence is that the Al^{VI}/Al^{IV} ratio increases with decreasing Al in the 'NaCr' dredges, whereas it slightly decreases in the global set (Fig. 8I).

Binary cationic plots are assumed to reflect the variations of the molecular components (or substitutions) that operate within the pyroxenes during magmatic, metasomatic and/or cooling processes. Molecular components of the clinopyroxenes of the two SWIFT extreme compositions (SWF-26-2-5 and SWF-26-2-7) were calculated on the basis of six oxygen atoms and normalized to four cations excluding Mn and Ni; no determination of Fe^{3+} was attempted. Seven components were considered: jadeite

$NaAl^{VI}Si_2O_6$ (Jd), kosmochlor $NaCrSi_2O_6$ (Ko), the Tschermak's molecules, $CaCrSiAl^{IV}O_6$ (CaCrTs), $CaAl^{VI}SiAl^{IV}O_6$ (CaTs) and $CaTiAl^{IV}{}_2O_6$ (CaTiTs), $Ca(Mg + Fe)Si_2O_6$ (DiHd) and $(Mg + Fe)_2Si_2O_6$ (EnFs). Because Na and Cr are involved in three components (Jd, Ko, CrTs), molecular proportions are not unique for a given cationic composition and the Jd/Ko ratio cannot be precisely determined. Two endmembers have been calculated (Table 4). In calculation (1) the Jd component is assumed equal to the maximum available Na; there is no Ko component and the CaTs is equal to remaining Al^{VI}. In calculation (2) all Cr is combined with Na to form the Ko component and remaining Na is assigned to Jd. The other components are calculated according to Mollo et al. (2013). After forming all the components Si shows a negative balance of 0.017 cations for SWF-26-2-5 and 0.008 cations for SWF-26-2-7, indicative of a slight charge disequilibrium; as Fe^{3+} must be very small, this disequilibrium is ascribed to analytical uncertainty on the Si/Al ratio. For a given chemical composition, varying the distribution of Na and Cr among Jd, Ko and CrCaTs has no effect on the total Tschermak's molecules and on the Ca-Mg-Fe components. Calculation (1) gives the maximum Jd and the minimum CaTs; calculation (2) the minimum Jd and the maximum CaTs. The linear trends shown in Fig. 8 are thus independent of the Jd/Ko ratios and give no information on the relative behaviour of the sodic components during magmatic and post-magmatic processes. However, the amount of Ko, being limited by available Cr, cannot be > 2.3 mol.% in SWF-26-2-5 clinopyroxene (for Jd + Ko = 3.1 mol.%) and > 5.2 mol.% in SWF-26-2-7 clinopyroxene (for Jd + Ko = 10.1 mol.%). Calculation (2) allows a near equal partioning of Na between Jd and Ko in SWF-26-2-7 clinopyroxenes (Table 4). In all cases, clinopyroxene evolution from SWF-26-2-5 to SWF-2-2-7 involves a strong increase in the sodic components and decrease in the Tschermak's molecules, whereas the sum of the Ca-Mg-Fe components remains nearly stable (or decreases very slightly). The good negative correlation between Na + Cr and Ca +Mg (Fig. 8K) may indicate that the coupled substitution, Na + Cr = Ca + Mg (i.e., Ko = Di) was active in the clinopyroxenes of the 'NaCr' dredges (Ikehata and Arai, 2004). However, calculation (1) which assigns Cr in CaCrTs alone (no Ko) also reproduces a 'NaCr' trend nearly parallel to the Ko = Di line. The whole of compositional variations observed from SWF-26-2-5 to SWF-26-2-7 suggests that the most robust substitution is the replacement of Ca by Na in the octahedral site. Strong increase in Na combined with Al depletion significantly modify the Al^{VI}/Al^{IV} ratios, leading to a negative correlation between Al^{VI}/Al^{IV} and Al and a positive correlation between Na and Cr, even if there is no Ko component.

4.4. Trace element geochemistry in pyroxenes of dredge SWF-26 peridotites

Trace element analyses performed in cores and rims of clinopyroxenes show that the grains are unzoned and display no significant differences from grain to grain at thin section and sample scales (Fig. 9; Supplementary Data Table S1). The two lherzolites SWF-26-2-5 and SWF-26-2-9 and the harzburgite SWF-26-2-7 are characterized by flat heavy REE (HREE) patterns (Dy_N/Yb_N =1.05–1.08) with depletions in light REE (LREE), varying from high (e.g., La_N/Yb_N = 0.002–0.007) in the lherzolites to moderate (e.g., La_N/Yb_N = 0.041) in the harzburgite. There is no correlation between modal clinopyroxene contents and REE concentrations: the clinopyroxene-rich lherzolite SWF-26-2-5 and the harzburgite have similar HREE concentrations (e.g., Yb_N = 2.7), while the lherzolite SWF-26-2-9 have high REE contents (e.g., Yb_N = 8.7). In the third lherzolite (SWF-26-2-11) normalized REE concentrations decrease almost linearly from the HREE (e.g., Yb_N = 5.6) to Nd (Nd_N/Yb_N = 0.19), followed by a stronger depletion in LREE (La_N/Sm_N = 0.06; La_N/Yb_N = 0.02). The shapes of the REE patterns are comparable with those of the lherzolites sampled along the SWIR axis east of the Melville FZ (Fig. 9), although the SWF-26-2-5 patterns are shifted to lower REE concentrations. SWF-26-2-7 (Fig. 9B) differ from the harzburgites sampled west of the Melville FZ. Its unusual REE patterns, characterized by a small peak in Eu, was also reported in clinopyroxenes highly enriched in Na and Cr in EDUL Dr6-1-1 (Fig. 9B) and in PS55-90-21A (not shown) from Lena Trough (Hellebrand and Snow, 2003); in both dredge sites these samples coexist with peridotites showing clinopyroxene REE patterns equilibrated with an alkaline melt (Seyler et al., 2011; Hellebrand and Snow, 2003). In dredge SWF-26 clinopyroxenes, as well as in other 'NaCr' dredges, the most incompatible trace elements Ce, Sr and Zr (Fig. 10A–C) and Nb (not shown) increase with increasing Na_2O and decreasing Al_2O_3 (Supplementary Data Fig. S3A–C). In contrast, the less incompatible elements Ti, Dy and Yb (Fig. 10E–F) and Y (not shown) show no correlation with Na_2O but are better correlated with Al_2O_3 (i.e., concentrations globally decrease with decreasing Al_2O_3, see Supplementary Data Fig. S3D–F). It thus appears that in 'NaCr' dredges, the more incompatible elements (e.g., Ce, Sm) are decoupled from the less incompatible elements (e.g., Yb) and their ratios tend to increase with increasing Cr#. Fig. 9 shows that the four SWF-26 REE patterns cannot be related to each other by a simple fractional melting process in closed system. These two points can also be expressed as variations of Sm_N/Yb_N and Ce_N/Yb_N as a function of Yb_N where these samples define a broad crosscutting trend with respect to pure fractional melting trends (Supplementary Data Fig. S4).

Orthopyroxene trace element concentrations were not analyzed in SWF-26-2-11 due to alteration. In the other samples orthopyroxene show typical REE patterns characterized by steep slopes. As for clinopyroxenes, SWF-26-2-5 orthopyroxene has lower bulk REE concentrations (Yb_N = 0.71) than SWF-26-2-9 (Yb_N = 2.3) for similar

LREE depletions (Ce_N/Yb_N = 0.001–0.002). Orthopyroxene REE slope in the harzburgite SWF-26-2-7 is less steep (Ce_N/Yb_N = 0.01) for Yb_N = 0.51.

5. Evidence for syn-melting metasomatism

Besides the effects of incomplete sub-solidus re-equilibration, modal and chemical variations of the sub-ridge lithospheric mantle on a scale < 1 km are attributed to two major late-stage and post-melting processes, namely the entrapment of unextracted melt and reactive porous flow (Brunelli et al., 2006; Elthon, 1992; Hellebrand et al., 2002a; Johnson and Dick, 1992; Warren and Shimizu, 2010). In most cases, these processes are identified by the decoupling between the major elements indicators of melting, such as Cr# in spinel and pyroxenes, and the highly incompatible trace elements, such as LREE, Sr and Zr. In the same way, Na_2O contents measured in clinopyroxenes are generally higher than expected for a residual phase, and considered as a marker of a refertilization event (Elthon, 1992). Examples of dredge-scale enrichments in Na_2O and highly incompatible trace elements in clinopyroxenes have been reported by Hellebrand et al. (2002a) in lherzolites and harzburgites from the Central Indian ridge (CIR). The authors proposed a model of refertilization by inefficiently extracted melt which crystallizes as clinopyroxene films on olivine–orthopyroxene grain boundaries. This model is similar to that developed by Elthon (1992) to explain the excess of Na_2O in abyssal peridotites with respect to fractional depletion trends. Using a simple mixing model, Hellebrand et al. (2002a) calculated that addition of 0.5–1 wt.% instantaneous melt produced after 12% critical melting of the depleted MORB mantle (DMM) with 0.5% residual melt porosity to a highly depleted, refractory harzburgite (0.1% modal residual clinopyroxene) has for effect to increase by a factor of ~16 the Ce_N/Yb_N ratio in the clinopyroxenes of harzburgites from dredge CIRCE 93 (CIR axis ~12°S) after crystallization and re-equilibration. The authors did not calculate the enrichment in Na_2O, but it can be argued that the refertilizing melt used in their model is too depleted in Na_2O (< 1 wt.%) and/or added in too small amount to increase the clinopyroxene Na_2O content from 0.1 wt.% (sample CIRCE 93-4) to 0.66 wt.% (sample CIRCE 93-7). Bulk Na_2O concentrations calculated with the modes and mineral compositions given by Hellebrand et al. (2002a) lead to 0.009 wt.% Na_2O in CIRCE 93-4 and 0.017 wt.% Na_2O in CIRCE 93-7. Using Elthon (1992) and Hellebrand et al. (2002a)'s entrapment model (i.e. crystallization of all the trapped melt to form 70% olivine + 30% clinopyroxene, followed by redistribution of Na_2O between the two pyroxenes upon re-equilibration of the modified peridotite) we calculated that the observed Na_2O increase in clinopyroxenes of the CIRCE samples requires a refertilizing melt containing ~5 wt.% Na_2O when 0.99 depleted harzburgite mix with 0.01 melt. Adding 1–2% of enriched MORB or alkali-basalt (2–3 wt.% Na_2O) will also reproduce the Na_2O increase. Because melt is strongly enriched in Al_2O_3 and depleted in Cr_2O_3 with respect to the residual peridotite, Cr# should decrease in the re-equilibrated peridotite, although calculation shows that Cr# reduction is negligible for melt addition < 2% vol. Cr# in minerals is proportional to the bulk Cr#, therefore clinopyroxene Cr# will decrease or remain nearly constant while Na_2O concentration increases. Entrapment model thus cannot explain the large and concomitant variations in Na_2O and Cr# observed in the clinopyroxenes of the 'NaCr' peridotites, although it may work for moderate Na_2O enrichment with no significant modification in the major elements indicators of melting.

Reactive porous flow is another process that leads to selective enrichments in incompatible elements (Vernières et al., 1997), triggered by melt infiltration from a nearby melt channel (Kelemen et al., 1992; Lundstrom, 2000, 2003) or upward advective transport of intergranular partial melts (Godard et al., 1995; Brunelli et al., 2006). In a melting column, incompatible trace elements can be fractionated in the same way as for the chromatographic columns: during upward melt migration incompatible elements are modulated according to their partition coefficients (Liang and Parmentier, 2010), leading to preferential enrichments in LREE relative to HREE or spoon-shaped REE patterns in bulk rock and clinopyroxene (Hellebrand et al., 2002a; Warren and Shimizu, 2010). Melt infiltration through the shallow mantle can also create centimeter-scale major element variations; one of the best examples are the variations of TiO_2 and Na_2O concentrations (Dick et al., 2010; Paquet et al., 2016). On the contrary, dredge SWF-26 clinopyroxenes have homogeneous Ti, Na and trace element compositions at the sample scale and REE patterns showing no preferential LREE enrichments over HREE. These features attest for melt-rock equilibration occurring at high temperature because, over small length-scales, incompatible element variations cannot be preserved for long time (e.g. 41 Myr, Warren and Shimizu, 2010). Consistently, temperatures derived from the REE-in-two-pyroxene thermometer of Liang et al. (2013) average 1206 ± 53°C at 1.2 GPa, in the same range as other abyssal peridotites unaffected by post-melting metasomatism (Liang et al., 2013).

Several lines of evidence point to an origin mostly controlled by melting and melt extraction for the dredge SWF-26 peridotites: (i) the samples lack of petrographic evidence for late-stage magmatic crystallization and veining and display microstructures similar to those of the abyssal peridotites considered as “purely residual”; (ii) spinels contain < 0.1 wt.% TiO_2 and clinopyroxenes are depleted in LREE relative to HREE; (iii) Al_2O_3 contents in pyroxenes, Cr# in spinel and modal proportions of the mineral phases are correlated. Because Na, LREE, Sr, Zr and Nb of the clinopyroxenes increase with increasing extent of melting, we conclude that refertilization and partial melting (or at least part of the partial melting) were two linked processes that have occurred simultaneously.

6. Modelling concomitant sodium and chromium enrichments in clinopyroxenes

Here we model the variations of Na_2O in clinopyroxenes during partial melting of a peridotite with an incremental open-system melting model, which assumes that a melt enriched in incompatible elements enters the system during the melting process (Ozawa and Shimizu, 1995; Brunelli et al., 2014). The model assumes Na behaving as a dilute element and uses the equations, melting modes and dynamic parameters of Brunelli et al. (2014). Initial mode (spinel-equilibrated) and Na_2O concentrations (0.13 wt.%) of the DMM are from Workman and Hart (2005). Sodium partition coefficient between clinopyroxene and melt (D_{cpx}^{Na}) has been shown to be strongly pressure-dependent, becoming more compatible with pressure and reaching the unity at around 3 GPa in mafic systems (see the compilation of Bedard, 2014 and references therein). In order to reproduce the behaviour of Na during melting we performed several calculations varying D_{cpx}^{Na} ; this parameter is assumed constant for every calculation thus simulating an isobaric process. Sodium partition into orthopyroxene is shown to be independent from P, T and composition (Kinzler, 1997; Kinzler et al., 1992), averaging 0.05 with little variability. We assumed this value in all our calculations. The composition of the residual clinopyroxene is related to the composition of the residual peridotite by $C_{cpx} = C_S(D_{cpx}^{Na}/D_{bulk}^{Na})$, where C_S is the composition of the solid in equilibrium with the liquid and D_{bulk}^{Na} the bulk partition coefficient for Na. The reader is referred to Brunelli et al. (2014) for a complete description of the model and system of equations.

In spinel-equilibrated peridotites the incremental degree of melting can be expressed in term of Cr# in bulk rock that is partitioned between the two pyroxenes and spinel phases. Based on a global correlation between spinel and clinopyroxene Cr-Al distribution, the correlation between Cr# in spinel and Cr# in clinopyroxene can be expressed as: $Cr\#_{cpx} = 4.64 + 0.34Cr\#_{sp}$ ($r^2 = 0.95$)[1] (Brunelli et al., in prep.). The correlation between spinel Cr# and the degree of melting is expressed by Hellebrand et al. (2001) as $F_{sp}= 0.1\ln(Cr\#_{sp}) + 0.24$ [2]. Inverting equation [2] and integrating with [1] allows calculating the expected Cr# of the clinopyroxene for the model incremental degree of melting (Brunelli et al., in prep). Na_2O concentrations can thus be plotted versus Cr# of the clinopyroxene as a proxy of the incremental degree of melting.

Hereafter we assumed a variable critical mass porosity (φ_c). The critical mass porosity represents the threshold value for the porosity interconnection and hence melt extraction (Zou, 1998). Fractional melting corresponds to $\varphi_c = 0$ while batch melting $\varphi_c = 1$ (Zou, 1998). Brunelli et al. (2014) upgraded this model by considering intermediate values of φ_c allowing the exploration of intermediate states between batch and fractional when considering an open melting system. In this model, the notation φ_c/F represents the ratio between the critical porosity and the degree of melting for a given melting cell; this ratio is a proxy of the batch character of the melting process becoming closer to pure fractional at low values ($\varphi_c/F \rightarrow 0$) or to batch melting for high values ($\varphi_c/F \rightarrow 1$). In a fractional melting scenario, ($\varphi_c/F = 0$; Fig. 11A), the main trend of the abyssal peridotite is bracketed by values of D_{cpx}^{Na} ranging 0.3–0.6, corresponding to 1.7-3.0 GPa melting pressure according to Bedard (2014)'s regression. When considering melting in a dynamic system (i.e. accounting for variable residual porosity) the main trend can be matched by lower values of D_{cpx}^{Na} thus melting at lower pressures. In Fig. 11B we have used a dynamic fractional melting where melt is partially retained in the source thus increasing the batch behaviour of the process (see discussion in Brunelli et al., 2014). In this case the base trend is bracketed by D_{cpx}^{Na} values between 0.1–0.3. Based on the regression of Bedard (2014) these values cover the entire pressure range from the crust to 1.7 GPa. Inversion from D_{Na} to pressure gives, however, just a rough value because of the large variability in each experimental dataset and global scatter.

Melting under dynamic conditions also reveals that the Na content of the residual clinopyroxene can be strongly enriched when the system behaves with a more batch character (high φ_c/F values). However a better match of the observed Na_2O–Cr# trend requires lowering the Na content of the source along with increasing the batch character of the process. In Fig. 11C, we observe that the Na_2O–Cr# trend is well matched by assuming the source to be more Na-depleted than DMM, down to 0.08 Na_2O wt.% in the source. With that value the Na_2O–Cr# trend can be matched by increasingly higher φ_c/F values i.e. toward more batch conditions. The higher is the batch character of the process the lower is the required Na partition, hence the inferred pressure of the process. According to the calibration of Bedard (2014), it appears that the inferred pressure values are deeper than 3 GPa, well inside the garnet stability field. High degrees of melting in the garnet field are however not recorded in the trace element patterns of the residual clinopyroxenes (Fig. 9) nor admitted by the low thermal setting of the region. From this simple modelling it also appears that the depth of the process and its exact nature (φ_c/F) cannot be determined contextually.

We now assume that an exotic melt enters the system during the melting process. The parameter β represents the influx rate of the exotic melt. The composition of the melt cannot be defined *a priori* hence we run some calculations at variable sodium content. It appears that liquids having MORB composition (Na_2O < 2 wt.%) do not modify substantially the trends derived for dynamic systems. When instead considering high Na melts (Na_2O ≥ 3 wt.%) the Na_2O–Cr# trend appears to be matched at progressively low pressures (lower D_{cpx}^{Na}) and more fractional conditions. In Fig. 12 we report the model results for melting in open-system with influx of a Na-rich melt (Na_2O = 4 wt.%) comparable to the high pressure melts hypothesized by Lundstrom (2000). We fixed the incoming rate at $\beta = 0.2$ and vary D_{cpx}^{Na} and the nature of the process from near-batch to near-fractional. It appears that the Na_2O–Cr# trend can be matched at lower pressures (lower D_{cpx}^{Na}) with respect to the dynamic case. Trace element distribution in clinopyroxene vary coherently with the Na enrichment showing high LREE/HREE ratios (Supplementary Data Fig. S4). These values have been shown to derive from garnet field-derived melts entering the system under open-system conditions by Brunelli et al. (2014), thus confirming the high pressure character of the inflowing melt.

Modelling under open-system melting conditions suggests therefore that when relatively high Na melts enter the melting system the residual pyroxenes can be progressively enriched in Na when the system tends to near-batch conditions. However, even in case of near-fractional processes, the simple incoming of Na-rich melts can produce the observed scatter in the global set for residual mid-ocean ridge clinopyroxenes.

7. Discussion

Melts produced by partial melting in the upwelling mantle ascent more rapidly than the surrounding solid matrix; they are channelized in the shallow mantle where partial melts aggregate and are transported to the surface (Kelemen et al., 1992). Melt channelling introduces substantial horizontal variations in the composition of the surrounding, partially molten peridotite, due to mineral reactions triggered by the differences of chemical compositions between the melt within the channel and the intergranular partial melt in equilibrium with the residual peridotite (Liang and Parmentier, 2010). On one hand, high-pressure melts are poorer in SiO_2 relative to late-stage melts because the olivine stability field expands at the expenses of orthopyroxene with decreasing pressure (Stolper, 1980). Consequently, reactions between high-pressure melts undersaturated in orthopyroxene and peridotite equilibrated at low pressure may significantly modify the peridotite mode by orthopyroxene resorption and olivine precipitation (Daines and Kohlstedt, 1994; Kelemen et al., 1992). In another hand, early melts generated at greater depth from a more fertile lithology are also richer in Na_2O and incompatible trace elements than interstitial melts in equilibrium with the residual peridotite at lower depth. The infiltration–reaction experiments of Lundstrom (2000, 2003) have shown that Na diffuses rapidly in response to gradients in silica activity from the SiO_2-poor/Na_2O-rich melt into the adjacent partially molten peridotite. The incongruent nature of the orthopyroxene melting results in an increase of the residual olivine and contextually leads to an increase in the silica content of the produced melt which in turn increases the diffusion rate of Na (Lundstrom, 2000). In Lundstrom's experiments this melting reaction is attested by changes in mineral modes (decrease in orthopyroxene, increase in olivine and melt) and mineral compositions (increasing Cr and decreasing Al^{VI} in clinopyroxene; increasing Cr# and decreasing Mg#

in spinel). In addition, the bulk content of Na_2O is increased in the diffusively infiltrated peridotite, so that subsolidus re-equilibration of the peridotite with some amount of unextracted melt will result in a peridotite significantly enriched in Na_2O. This process may be an alternative to the refertilization by addition of melt (Elthon, 1992) to explain Na enrichment in 'normal' abyssal peridotites. However it is insufficient to produce extreme enrichments in both Na and Cr.

From these observations we infer that high Na_2O concentrations can be reached in the infiltrated peridotite when a Na-rich or alkaline melt is reinjected in the melting peridotite after (partial) extraction of the preceding melt batch. Increased Na content lowers the silica activity coefficient in the melt (Lundstrom, 2003 and references therein). Thus mixing a Na-rich melt with the tholeiitic melt in equilibrium with the peridotite would shift the olivine - orthopyroxene phase boundary, increasing the peridotite incongruent melting and leading to Al-poorer, Cr-richer residues significantly enriched in Na. Diffusion of Na (through Ca - Na exchange reaction?) from nearby channels transporting alkaline melt/fluid into the partially molten peridotite may have similar effects. As shown in Fig. 4–8, the compositional relationships within the peridotites from dredge SWF-26 may well illustrate the process of Na diffusion during upwelling of the asthenospheric mantle beneath the SWIR section of this study.

Chemical modelling discussed in the previous paragraph suggests that low amounts of high pressure melts enter the spinel-field melting region. High Na and concomitant crosscutting trends in the Sm/Yb vs. Yb compositional space (Supplementary Data Fig. S4) are suggestive for a garnet field origin of the infiltrating melt as discussed by Seyler et al. (2011) and Brunelli et al. (2014). These melts require a fertile, low-solidus, source lithology possibly represented by dispersed pyroxenitic bodies in the peridotitic mantle screen. Melts produced this way are easily channelized in the shallow mantle where partial melts aggregate and are transported to the surface (Katz and Weatherley, 2012).

8. Summary and concluding remarks

1- Mantle-derived peridotites dredged at the SWIR axis between Discovery and Indomed FZs display a spectrum of modal and mineral major element compositions at all length scales, spanning the whole compositional range of abyssal, residual spinel peridotites. Large major element compositional variations at the scale of a dredge site are common at ultra-slow spreading ridges and reflect high extent of melt-rock interaction by focused melt transport and mantle source heterogeneities.

2- Clinopyroxene compositions in the four analyzed samples of SWIFT dredge 26 and similar samples identified in other few regions of ultra-slow spreading ridges define compositional trends atypical of residual abyssal peridotites, characterized by concurrent increases in sodium and chromium concentrations while aluminum decreases, leading to extreme enrichments in both elements (up to 1.7 wt.% Na_2O and up to 2.1 wt.% Cr_2O_3). Despite this odd behaviour, the petrography (microstructures) and other geochemical features (such as, high depletion in LREE/HREE and very low Ti contents in pyroxenes and spinel) are typical of residual peridotites.

3- The positive correlation between Na and Cr does not necessary reflect a kosmochlor component, but may result from the fact that the Al-Tschermak's molecule decreases more rapidly than the sodic components (Jd ± Ko), leading to inverse correlation between octahedral and tetrahedral Al. Assuming that Al depletion and increasing Cr# in pyroxenes and spinel reflect increasing melt depletion in the peridotites, our modelling suggests that similar clinopyroxene compositional variation can be reproduced when Na is added during partial melting of the peridotite. This may involve upward percolation of a Na-rich melt derived from melting of low-solidus heterogeneities, or, alternatively, diffusion of Na from nearby melt channels into the partially molten peridotite during mantle upwelling, as suggested by Lundstrom (2000). Both explanations are consistent with the compositions of the associated basalts, which vary from normal-MORB to enriched MORB and alkali-basalts.

4- In clinopyroxenes of the global abyssal peridotite set, Na_2O is positively correlated with the abundances of incompatible trace elements. However, in the dredges in which Na and Cr in clinopyroxenes are positively correlated, Na_2O is correlated only with highly incompatible trace elements (e.g., Sr, Zr, Nb, LREE), whereas the less incompatible elements (e.g., Ti, Y, HREE) tend to remain nearly constant or to decrease. We can predict that the study of a larger sample set and consideration of trace element behaviour will add more complexities to the present model. In this study, clinopyroxene major elements define uniform compositional trends because they are also controlled by the crystal structure, while trace element ratios will reflect different melt composition, pre-existing mantle heterogeneities and/or different melting parameters.

Acknowledgements

Funding for this research was provided by Centre National de la Recherche Scientifique-Institut National des Sciences de l'Univers. DB is supported by Programma di Rilevante Interesse Nazionale-PRIN prot.2015C5LN35 and by PNRA project 2016_00245. We are grateful to Olivier Bruguier for his help in the acquisition and interpretation of the LA-

ICPMS analyses and to Bernard Boyer for his technical assistance with the SIMS analyses. Philippe Recourt is thanked for the SEM-EDS assistance and Michel Fialin for the EMPA assistance. The manuscript has been substantially improved after thorough reviews by an anonymous reviewer.

References

Agar, S.M., Lloyd, G.E., 1997. Deformation of Fe-Ti oxides in gabbroic shear zones from the MARK area. In: Kanson, J.A., Cannat, M., Miller, D.J., Elthon, D. (Eds), Proceedings of the Ocean Drilling Program (ODP), Scientific Results Vol. 153. College Station, TX, pp. 123–142.

Anders, E., Grevesse, N., 1989. Abundances of the elements: meteoritic and solar. Geochimica et Cosmochimica Acta 53, 197–214.

Aslanian, D., Humler, E., Michel, E., 2002. MD 125 / SWIFT BIS-CARHOT cruise, RV Marion Dufresne, http://dx.doi.org/10.17600/2200020.

Bédard, J.H., 2014. Parameterizations of calcic clinopyroxene–melt trace element partition coefficients. Geochemistry, Geophysics and Geosystems 15 (2), 303–336.

Bezos, A., Lorand, J.-P., Humler, E., Gros, M., 2005. Platinum-group element systematics in mid-ocean ridge basaltic glasses from the Pacific, Atlantic and Indian Oceans. Geochimica et Cosmochimica Acta 69, 2613–2627.

Brey, G., Köhler, T., 1990. Geothermobarometry in four-phase lherzolites II. New thermobarometers, and practical assesment of existing thermobarometers. Journal of Petrology 31, 1353-1378.

Brunelli, D., Seyler, M., 2010. Asthenospheric percolation of alkaline melts beneath the St. Paul region (Central Atlantic Ocean). Earth and Planetary Science Letters 289 (3–4), 393–405.

Brunelli, D., Seyler, M., Cipriani, A., Ottolini, L., Bonatti, E., 2006. Discontinuous melt extraction and weak refertilization of mantle peridotites at the Vema Lithospheric Section (Mid-Atlantic Ridge). Journal of Petrology 47 (4), 745–771.

Brunelli, D., Paganelli, E., Seyler, M., 2014. Percolation of enriched melts during incremental open-system melting in the spinel field : a REE approach to abyssal peridotites from the Southwest Indian Ridge. Geochimica et Cosmochimica Acta 127, 190–203.

Ceuleneer, G., Cannat, M., 1997. High-temperature ductile deformation of site 920 peridotites. In: Kanson, J.A., Cannat, M., Miller, D.J., Elthon, D. (Eds), Proceedings of the Ocean Drilling Program (ODP), Scientific Results Vol. 153. College Station, TX, pp. 23–34.

Ceuleneer, G., Nicolas, A., Boudier, F., 1988. Mantle flow patterns at an oceanic spreading centre: the Oman peridotite record. Tectonophysics 151, 1–26.

Chauvel, C., Blichert-Toft, J., 2001. A hafnium isotope and trace element perspective on melting of the depleted mantle. Earth and Planetary Science Letters 190, 137–151.

Cipriani, A., Bonatti, E., Brunelli, D., Ligi, M., 2009. 26 million years of mantle upwelling below a segment of the Mid Atlantic Ridge: The Vema Lithospheric Section revisited. Earth and Planetary Science Letters, 285 (1), 87-95.

Cipriani, A., Brueckner, H.K., Bonatti, E., Brunelli, D., 2004. Oceanic crust generated by elusive parents: Sr and Nd isotopes in basalt–peridotite pairs from the Mid-Atlantic Ridge. Geology 32 (8), 657–660.

Daines, M.J., Kohlstedt, D.L., 1994. The transition from porous to channelized flow due to melt/rock reaction during melt migration. Geophysical Research Letters 21 (2), 145–148.

DeMets, C., Gordon, R.G., Argus, D.F., Stein, C., 1990. Current plate motion, Geophysical Journal International 101, 425–478.

D'Errico, M.E., Warren, J.M., Godard, M., 2016. Evidence for chemically heterogeneous Arctic mantle beneath the Gakkel Ridge. Geochimica et Cosmochimica Acta 174, 291–312. http://dx.doi.org/10.1016/j.gca.2015.11.017.

Dick, H.J.B., Bullen, T., 1984. Chromian spinel as a petrogenetic indicator in abyssal and alpine-type peridotites and spatially associated lavas. Contributions to Mineralogy and Petrology 86, 54–76.

Dick, H.J.B., Lissenberg, C.J., Warren, J.M., 2010. Mantle melting, Melt transport, and delivery deneath a slow-spreading ridge: The Paleo-MAR from 23°15'N to 23°45'N. Journal of Petrology 51, 425–467.

Dick, H.J.B., Ozawa, K., Meyer, P.S., Niu, Y., Robinson, P.T., Constantin, M., Hebert, R., Maeda, J., Natland, J.H., Hirth, J.G. and Mackie, S.M., 2002. Primary silicate mineral chemistry of a 1.5-km section of very slow spreading lower ocean crust: ODP Hole 735B, Southwest Indian Ridge. In: Natland H., Dick, H.J.B., Miller, D.J., Von Herzen, R.P. (Eds), Proceedings of the Ocean Drilling Program (ODP) Scientific Results Vol. 176. College Station, TX, pp. 1–61.

Elthon, D., 1992. Chemical trends in abyssal peridotites: refertilization of depleted suboceanic mantle. Journal of Geophysical Research 97, 9015–9025.

Gautheron, C., Moreira, M., Gerin, C., Tassan-Got, L., Bezos, A., Humler, E., 2015. Constraints on the DUPAL anomaly from helium isotope systematics in the Southwest Indian mid-ocean ridge basalts. Chemical Geology 417, 163–172.

Godard, M., Bodinier, J.L., Vasseur, G., 1995. Effects of mineralogical reactions on trace element redistributions in mantle rocks during percolation processes: a chromatographic approach. Earth Planetary Science Letters 133, 449–461.

Hamelin, B., Allègre, C.J., 1985. Large scale regional units in the depleted upper mantle revealed by an isotope study of the Southwest Indian Ridge, Nature 315, 196–199.

Hanson, G.N., 1977. Geochemical evolution of the suboceanic mantle. Journal of the Geological Society 134 (2), 235–253.

Harvey, J., Gannoun, A., Burton, K.W., Rogers, N.W., Alard, O., Parkinson, I.J., 2006. Ancient melt extraction from the oceanic upper mantle revealed by Re–Os isotopes in abyssal peridotites form the Mid-Atlantic ridge. Earth and Planetary Science Letters 244, 606–621.

Hellebrand, E., Snow, J.E., 2003. Deep melting and sodic metasomatism underneath the highly oblique-spreading Lena Trough (Arctic Ocean). Earth and Planetary Science Letters 216, 283–299.

Hellebrand, E., Snow, J.E., Dick, H.J.B., Hofmann, A.W., 2001. Coupled major and trace elements as indicators of the extent of meting in mid-ocean-ridge peridotites. Nature 410, 677–681.

Hellebrand, E., Snow, J.E., Hoppe, P., Hofmann, A.W., 2002a. Garnet-field melting and late-stage refertilization in 'residual' abyssal peridotites from the Central Indian Ridge. Journal of Petrology 43 (12), 2305–2338.

Hellebrand, E., Snow, J.E., Mostefaoui, S., Hoppe, P., 2005. Trace element distribution between orthopyroxene and clinopyroxene in peridotites from the Gakkel Ridge: a SIMS and NanoSIMS study. Contributions to Mineralogy and Petrology 150, 486–504.

Hellebrand, E., Snow, J.E., Mühe, R., 2002b. Mantle melting beneath Gakkel Ridge (Arctic Ocean): abyssal peridotite spinel compositions. Chemical Geology 182 (2–4), 227–235.

Hirschmann, M.M., Stolper, E.M., 1996. A possible role for garnet pyroxenite in the origin of the "garnet signature" in MORB. Contributions to Mineralogy and Petrology 124, 185–208.

Humler, E., 2001. MD 121 / SWIFT cruise, RV Marion Dufresne, Reconnaissance géophysique de l'axe de la dorsale sud-ouest indienne et prélèvement de roches entre 33° E et 52° E. http://dx.doi.org/10.17600/1200030.

Ikehata, K., Arai, A., 2004. Metasomatic formation of kosmochlor-bearing diopside in peridotite xenoliths from North Island, New Zealand. American Mineralogist 89, 1396–1404.

Johnson, K.T.M., Dick, H.J.B., 1992. Open system melting and temporal and spatial variation of peridotite and basalt at the Atlantis II Fracture Zone. Journal of Geophysical Research 97 (B6), 9219–9241.

Katz, R.F., Weatherley, S.M., 2012. Consequences of mantle heterogeneity for melt extraction at mid-ocean ridges. Earth and Planetary Science Letters 335–336, 226–237.

Kelemen, P.B., Dick, H.J.B., Quick, J.E., 1992. Formation of harzburgite by pervasive melt/rock reaction in the upper mantle. Nature 358, 635–641.

Kinzler, R.J., 1997. Melting of mantle peridotite at pressure approaching the spinel to garnet transition: Application to mid-ocean ridge basalt petrogenesis. Journal of Geophysical Research-Solid Earth, 102(B1), 853–874.

Kinzler, R.J., Grove, T.L., 1992. Primary Magmas of Mid-Ocean Ridge basalts 1. Experiments and Methods. Journal of Geophysical Research-Solid Earth, 97(B5), 6885–6906.

Koepke, J., Feig, S.T., Snow, J., 2005. Hydrous partial melting within the lower oceanic crust. Terra Nova 17, 286–291.

Lambart, S., Baker, M.B., Stolper, E.M., 2016. The role of pyroxenite in basalt genesis: Melt-PX, a melting parameterization for mantle pyroxenites between 0.9 and 5 GPa. Journal of Geophysical Research - Solid Earth 121, 5708–5735.

Lambart, S., Laporte, D., Provost, A., Schiano, P., 2012. Fate of pyroxenite-derived melts in the peridotitic mantle: thermodynamic and experimental constraints. Journal of Petrology 53 (3), 451–476.

Lambart, S., Laporte, D., Schiano, P., 2013. Markers of the pyroxenite contribution in the major-element compositions of oceanic basalts : Review of the experimental constraints. Lithos 160, 14–36.

Lassiter, J.C., Byerly, B.L., Snow, J.E., Hellebrand, E., 2014. Constraints from Os-isotope variations on the origin of Lena Trough abyssal peridotites and implications for the composition and evolution of the depleted upper mantle. Earth and Planetary Science Letters 403, 178–187.

LeRoex, A.P., Dick, H.J.B., Fisher, R.L., 1989. Petrology and geochemistry of MORB from 25°E to 46°E along the Southwest Indian Ridge: Evidence for contrasting style of mantle enrichment. Journal of Petrology 30, 947–986.

Liang, Y., Parmentier, E.M., 2010. A two-porosity double lithology model for partial melting, melt transport and melt–rock reaction in the mantle: mass conservation equations and trace element transport. Journal of Petrology 51 (1–2), 125–152.

Liang, Y., Peng, Q., 2010. Non-modal melting in an upwelling mantle column: steady-state models with applications to REE depletion in abyssal peridotites and the dynamics of melt migration in the mantle. Geochimica et Cosmochimica Acta 74, 321– 339.

Liang, Y., Sun, C., Yao, L., 2013. A REE-in-two-pyroxene thermometer for mafic and ultramafic rocks. Geochimica et Cosmochimica Acta 102, 246–260.

Liu, C.-Z., Snow, J.E., Hellebrand, E., Brügmann, G.E., von der Handt, A.B., Hofmann, A.W., 2008. Ancient, highly heterogeneous mantle beneath Gakkel ridge, Arctic Ocean. Nature 452, 311–316.

Luguet, A., Lorand, J.-P., Seyler, M., 2003. Sulfide petrology and highly siderophile element geochemistry of abyssal peridotites: a coupled study of samples from the Kane Fracture Zone (45°W 23°20N, MARK Area, Atlantic Ocean). Geochimica et Cosmochimica Acta 67 (8), 1553–1570.

Lundstrom, C., 2000. Rapid diffusive infiltration of sodium into partially molten peridotite. Nature 403, 527–530.

Lundstrom, C., 2003. An experimental investigation of the diffusive infiltration of alkalis into partially molten peridotite: Implications for mantle melting processes. Geochemistry, Geophysics and Geosystems 4 (9) 8614.

Mahoney, J.J., Natland, J.H., White, W.M., Poreda, R., Bloomer, S.H., Fisher, R.L., Baxter, A.N., 1989. Isotopic and geochemical provinces of the western Indian Ocean spreading centers. Journal of Geophysical Research. 94, 4033–4052.

Mallick, S., Dick, H.J.B., Sachi-Kocher, A., Salters, V.J.M., 2014. Isotope and trace element insights into heterogeneity of subridge mantle. Geochemistry, Geophysics, and Geosystems 15, 2438–2453.

Mallick, S., Standish, J.J., Bizimis, M., 2015. Constraints on the mantle mineralogy of an ultra-slow ridge: hafnium isotopes in abyssal peridotites and basalts from the 9–25°E Southwest Indian Ridge. Earth and Planetary Science Letters 410, 42–53.

Mével, C., 1997. Sampling the Southwest Indian Ridge: First results of the EDUL cruise (R/V Marion Dufresne II, August 1997). InterRidge News 6-2, 25–26.

Meyzen, C.M., Ludden, J.N., Humler, E., Luais, B., Toplis, M.J., Mével, C., Storey, M., 2005. New insights into the origin and distribution of the DUPAL isotope anomaly in the ocean mantle from MORB of the Southwest Indian Ridge. Geochemistry, Geophysics and Geosystems 6, 1–34.

Meyzen, C.M., Toplis, M.J., Humler, E., Ludden, J.N., Mével, C., 2003. A discontinuity in mantle composition beneath the southwest Indian ridge. Nature 421, 731–733.

Mollo, S., Putirka, K., Misiti, V., Soligo, M., Scarlato, P., 2013. A new test for equilibrium based on clinopyroxene-melt pairs: Clues on the solidification temperatures of Etnean alkaline melts at post-eruptive conditions. Chemical Geology 352, 92–100.

Müller, R.D., Royer, J.Y., Lawver, L.A., 1993. Revised plate motions relative to the hotspots from Atlantic and Indian ocean hotpot tracks. Geology 21, 275–278.

Natland, J.H., Dick, H.J.B., 2001. Formation of the lower ocean crust and the crystallization of gabbroic cumulates at a very slowly spreading ridge. Journal of Volcanology and Geothermal Research 110, 191-233.

Ozawa, K., Shimizu N., 1995. Open-system melting in the upper mantle: constraints from the Hayachine-Miyamori ophiolite, northeastern Japan. Journal of Geophysical Research 100, 22315–22335.

Nicolas, A., 1986. A melt extraction model based on structural studies in mantle peridotites. Journal of Petrology 27, 999–1022.

Paquet, M., Cannat, M., Brunelli, D., Hamelin, C, Humler, E., 2016. Effect of melt/mantle interactions on MORB chemistry at the easternmost Southwest Indian Ridge (61 to 67°E). Geochemistry, Geophysics and Geosystems 17 (11), 4605–4640.

Pertermann, M., Hirschmann, M.M., 2003. Partial melting experiments on a MORB-like pyroxenite between 2 and 3 GPa: constraints on the presence of pyroxenite in basalt source regions from solidus location and melting rate. Journal of Geophysical Research 108 (B2). http://dx.doi.org/10.1029/2000JB000118.

Salters, V.J.M., Dick, H.J.B., 2002. Mineralogy of the mid-ocean-ridge basalt source from neodymium isotopic composition of abyssal peridotites. Nature 418, 68–72.

Seyler, M., Bonatti, E., 1997. Regional-scale melt–rock interaction in lherzolitic mantle in the Romanche Fracture Zone (Atlantic Ocean). Earth and Planetary Science Letters 146, 273–287.

Seyler, M., Toplis, M.J., Lorand, J.-P., Luguet, A., Cannat, M., 2001. Clinopyroxene microtextures reveal incompletely extracted melts in abyssal peridotites. Geology 29 (2), 155–158.

Seyler, M., Cannat, M., Mével, C., 2003. Evidence for major-element heterogeneity in the mantle source of abyssal peridotites from the Southwest Indian Ridge (52° to 68°E). Geochemistry, Geophysics, and Geosystems 4 (2), 9101.

Seyler, M., Lorand, J.-P., Toplis, M.J., Godard, G., 2004. Asthenospheric metasomatism beneath the mid-ocean ridge: evidence from depleted abyssal peridotites. Geology 32 (4), 301–304.

Seyler, M., Lorand, J.-P., Dick, H.J.B., Drouin, M., 2007. Pervasive melt percolation reactions in ultra-depleted refractory harzburgites at the Mid-Atlantic Ridge, 15°20'N: ODP Hole 1274A. Contributions to Mineralogy and Petrology 153, 303–319.

Seyler, M., Brunelli, D., Toplis, M.J., Mével, C., 2011. Multiscale chemical heterogeneities beneath the eastern Southwest Indian Ridge (52°E–68°E): trace element compositions of along axis dredged peridotites. Geochemistry, Geophysics, and Geosystems 12 (9), Q0AC15.

Spiegelman, M., Kelemen, P.B., 2003. Extreme chemical variability as a consequence of channelized melt transport. Geochemistry, Geophysics, and Geosystems 4 (7), 1055.

Stracke, A., Bourdon, B., 2009. The importance of melt extraction for tracing mantle heterogeneity. Geochimica et Cosmochimica Acta 73, 218–238.

Stracke, A., Snow, J.E., Hellebrand, E., von der Handt, A., Bourdon, B., Birbaum, K., Günther, D., 2011. Abyssal peridotite Hf isotopes identify extreme mantle depletion. Earth and Planetary Science Letters 308, 359–368.

Stolper, E.M., 1980. A phase diagram for mid-ocean ridge basalts: Preliminary results and implications for petrogenesis. Contribution to Mineralalogy and Petrolology 74, 13-27.

Suhr, G., Kelemen, P., Paulick, H., 2008. Microstructures in Hole 1274A peridotites, ODP Leg 209, Mid-Atlantic Ridge: Tracking the fate of melts percolating in peridotite as the lithosphere is intercepted. Geochemistry, Geophysics and Geosystems 9 (8), Q03012.

Vernières, J., Godard, M., Bodinier, J.-L., 1997. A plate model for the simulation of trace element fractionation during partial melting and magma transport in the Earth's upper mantle. Journal of Geophysical Research 102 (B11), 2471–24784.

Warren, J.M., 2016. Global variations in abyssal peridotite compositions. Lithos 248-251, 193-219.

Warren, J.M., Shimizu, N., 2010. Cryptic variations in abyssal peridotite composition: evidence for recent melt–rock reaction at the ridge. Journal of Petrology 51, 395–423.

Warren, J.M., Shirey, S.B., 2012. Lead and osmium isotopic constraints on the oceanic mantle from single abyssal peridotite sulfides. Earth and Planetary Science Letters, 359–360, 279–293.

Warren, J.M., Shimizu, N., Sakaguchi, C., Dick, H.J.B., Nakamura, E., 2009. An assessment of upper mantle heterogeneity based on abyssal peridotite isotopic compositions. Journal of Geophysical Research 114 (B12203).

Weatherley, S.M., Katz, R.F., 2012. Melting and channelized magmatic flow in chemically heterogeneous, upwelling mantle. Geochemistry, Geophysics and Geosystems 13, Q0AC18.

Wood, D.A., 1979. A variably veined suboceanic upper mantle-genetic significance for mid-ocean ridge basalts from geochemical evidence. Geology 7, 499–503.

Workman, R.K., Hart, S.R., 2005. Major and trace element composition of the depleted MORB mantle (DMM). Earth and Planetary Science Letters 231, 53–72.

Zou, H., 1998. Trace element fractionation during modal and nonmodal dynamic melting and open-system melting: A mathematical treatment. Geochimica et Cosmochimica Acta, 62 (11), 1937–1945.

Figure captions

Fig. 1. Bathymetric map of the SWIR region between 43° and 46° E [GeoMapApp© (http://www.geomapapp.org/)]. Dredged peridotites of this study are marked with a green star. Dredged basalts (from literature) are marked with a red diamond.

Fig. 2. Ultramafic ternary plot of the studied peridotites. Primary modes were reconstructed by visual estimation on hand-sample slices completed by counting 10,000 to 12,000 points at 0.5 mm spacing on thin sections. All samples plot within the

lherzolite-harzburgite field of residual peridotites from the SWIR (grey dots, compilation from Warren, 2016).

Fig. 3. Representative SWIFT peridotite microstructures. A: Sample SWF-26-2-5 micrograph (crossed nicols) showing an elongated aggregate of clinopyroxene + orthopyroxene crystals. Field lengths are 20 x 9 mm. B: Sample SWF-26-2-7 SEM backscatter image of a medium-sized clinopyroxene within partially serpentinized olivine. Curved grain boundary, olivine-filled embayments and tiny interstitial elongations from grain tips are typical of abyssal peridotites. C: SWF-26-2-9 composite EDS mapping of bimineralic pyroxene aggregates with irregular shape boundaries: serpentinized olivine (Ol); orthopyroxene (Opx); clinopyroxene (Cpx); spinel (Sp). D: Sample SWF-26-2-9 micrograph (crossed nicols) showing a straight contact between a clinopyroxene crystal (Cpx) and an orthopyroxene crystal (Opx). The left and lower sides of the clinopyroxene are fragmented and twisted. Field length is 6.8 mm. E: Sample SWF-26-2-9 micrograph (crossed nicols) of a clinopyroxene aggregate. Contacts between the crystals are curvilinear and surrounded by tiny orthopyroxene grains. Field length is 1.5 mm. F: Sample SWF-26-2-5 micrograph (crossed nicols) showing interlocking contact between two clinopyroxene crystals; the contact is sealed by orthopyroxene neoblasts. Field length is 2.7 mm.

Fig. 4. Variations of major element compositions of orthopyroxenes and clinopyroxenes of SWIFT peridotites. Each spot represents a single analysis. Residual peridotites from the SWIR (compilation from Warren, 2016) are plotted in the background (grey spots).

Fig. 5. Variations of Na_2O against Al_2O_3 (A), Cr_2O_3 (B) and TiO_2 (C) in clinopyroxenes of SWIFT peridotites. Same legend as Fig. 4.

Fig. 6. Variations of Cr# as a function of Mg# in spinels of SWIFT peridotites. Same legend as Fig. 2.

Fig. 7. Variation of spinel Cr# against modal olivine (A) and modal clinopyroxene (B) in SWIFT peridotites. Same legend as Fig. 2.

Fig. 8. Average clinopyroxene core compositions (in number of atoms based on 6 oxygens) in the four SWF-26 peridotites. Compositions of clinopyroxenes of EDUL Dr6 (Seyler et al., 2003, 2011) and of Arctic (Gakkel Ridge and Lena Trough) peridotites are plotted for comparison. Blue dots in the background represent the global field of residual peridotites from all oceanic ridges (compilation from Warren, 2016). Gakkel Ridge data (HLY102-70 at ~87°N) are from D'Errico et al. (2016) and Hellebrand et al. (2005). Lena Trough data (PS55-90 and PS66-257 and 262 at ~81°N) are from Hellebrand and Snow (2003) and Lassiter et al. (2014). All Arctic samples are spinel lherzolites and harzburgites, except a spinel olivine-websterite from Gakkel Ridge (HLY102-70-34, D'Errico et al., 2016). Regression line 1 (red color) corresponds to SWF-26 clinopyroxenes; regression line 2 (dark blue) corresponds to the global peridotite trend. Reference lines ($y = x + 2$) in panels (J) and (K) are for the ideal

substitutions, Na + Al^{VI} = Ca + Mg and Na + Cr = Ca + Mg, respectively. The deviation from the line indicates involvement of other elements (components) such as Al, Al^{IV} and Fe.

Fig. 9. Rare earth element compositions of clinopyroxenes and orthopyroxenes in the four SWF-26 peridotites. Representative clinopyroxene compositions of EDUL peridotites dredged on the SWIR axis, east (E1, E2) and west (W) of the Melville FZ are plotted for comparison; dashed line in panel B represents sample EDUL Dr6-1-1 highly enriched in Na and Cr (data from Seyler et al., 2011). Normalization values are from Anders and Grevesse (1989). DMM clinopyroxene is from Workman and Hart (2005).

Fig. 10. Variations of incompatible trace element compositions (in ppm) as a function of Na_2O wt.% in clinopyroxenes of SWF-26 peridotites. Same legend as Fig. 8.

Fig. 11. Variations of Na_2O versus Cr# in residual clinopyroxenes computed under non-modal melting conditions. Melting process varies from near-fractional (A) to near-batch (B and C). In the three models, φ_c/F represents the ratio between the critical porosity and the degree of melting; the partition coefficients of Na between clinopyroxene and melt vary from 0.01 and 1.2 (see labels in panel B). Melting modes and dynamic parameters are from Brunelli et al. (2014). Cr# is modelled in reference to the correlation with Cr# in coexisting spinel and Hellebrand et al. (2001)'s relation between spinel Cr# and degree of melting (see text). The initial source composition (Na_2O = 0.13

wt.%) is from Workman and Hart (2005) in panels A and B., and Na_2O = 0.08 wt.% in panel C. Peridotite samples are represented as in Fig. 8.

Fig. 12. Variations of Na_2O versus Cr# in residual clinopyroxenes computed under open-melting conditions, during which a Na-rich melt (Na_2O = 4 wt.%) is influxed at the rate β = 0.2. The ratios φ_c/F vary from 0 to 1 (see labels in panel B), corresponding to a progressive shift of the melting process from near-fractional to near-batch conditions. Two values are considered for partitioning of Na between clinopyroxene and melt: 0.1 (A) and 0.3 (B). The initial source composition (Na_2O = 0.13 wt.%) is from Workman and Hart (2005).

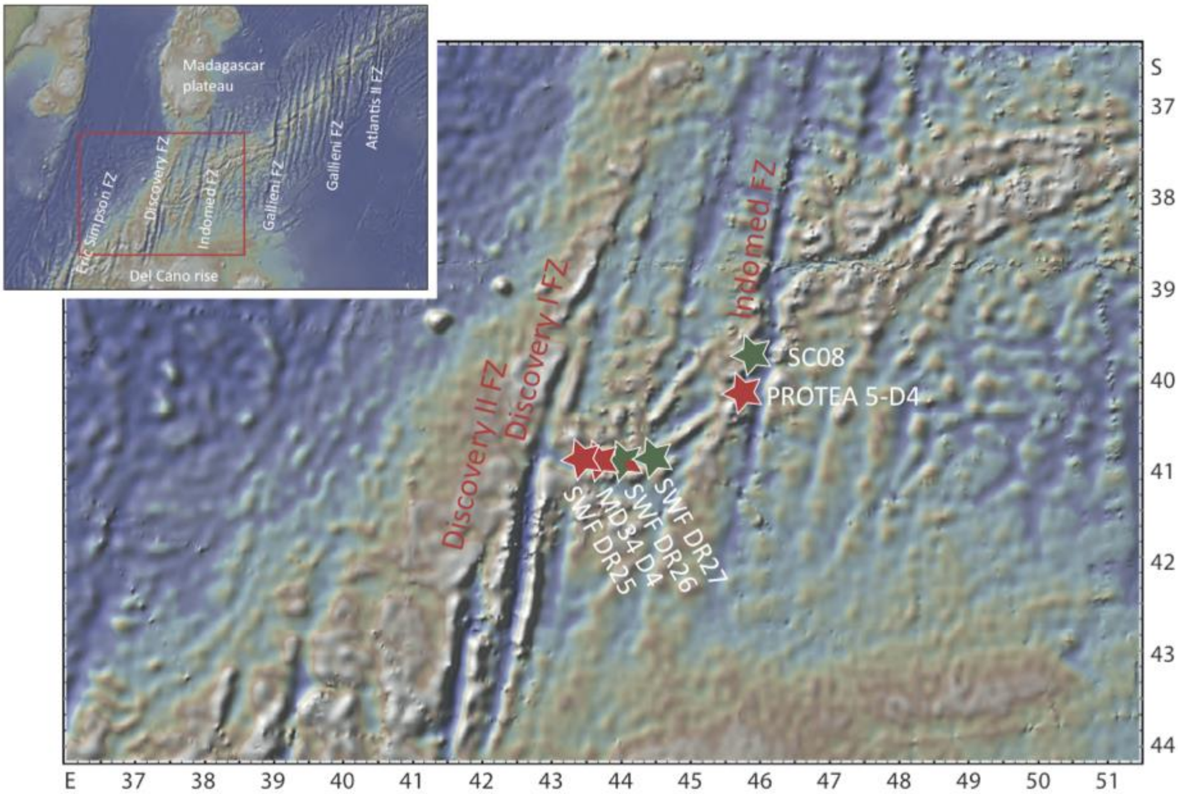
Madagascar plateau
Eric Simpson FZ
Discovery FZ
Indomed FZ
Gallieni FZ
Gallieni FZ
Atlantis II FZ
Del Cano rise
Discovery II FZ
Discovery I FZ
Indomed FZ
SC08
PROTEA 5-D4
SWF DR25
MD34 D4
SWF DR26
SWF DR27
S
37
38
39
40
41
42
43
44
E
37
38
39
40
41
42
43
44
45
46
47
48
49
50
51

Figure 1

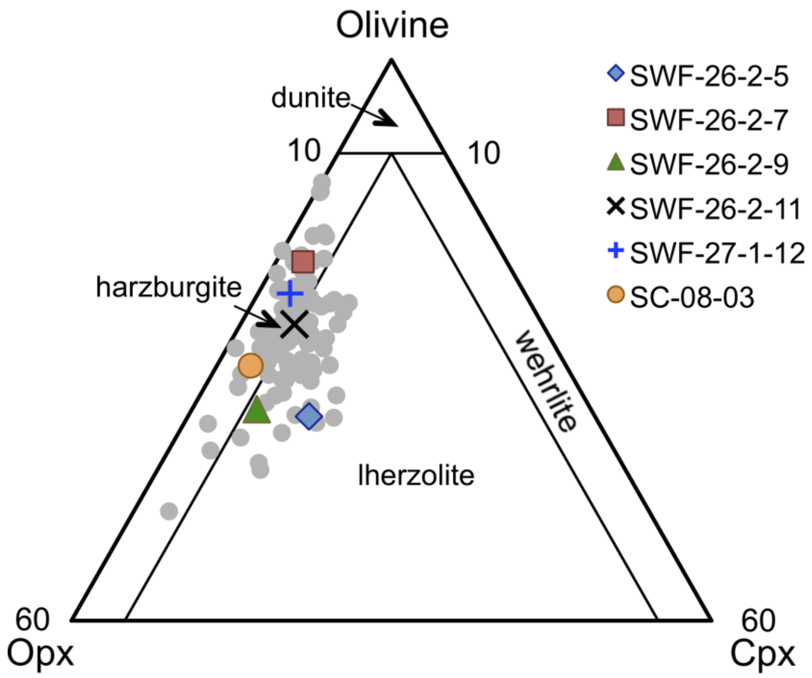
Olivine
dunite
10
10
harzburgite
wehrlite
lherzolite
60
Opx
60
Cpx
◆ SWF-26-2-5
■ SWF-26-2-7
▲ SWF-26-2-9
× SWF-26-2-11
+ SWF-27-1-12
● SC-08-03

Figure 2

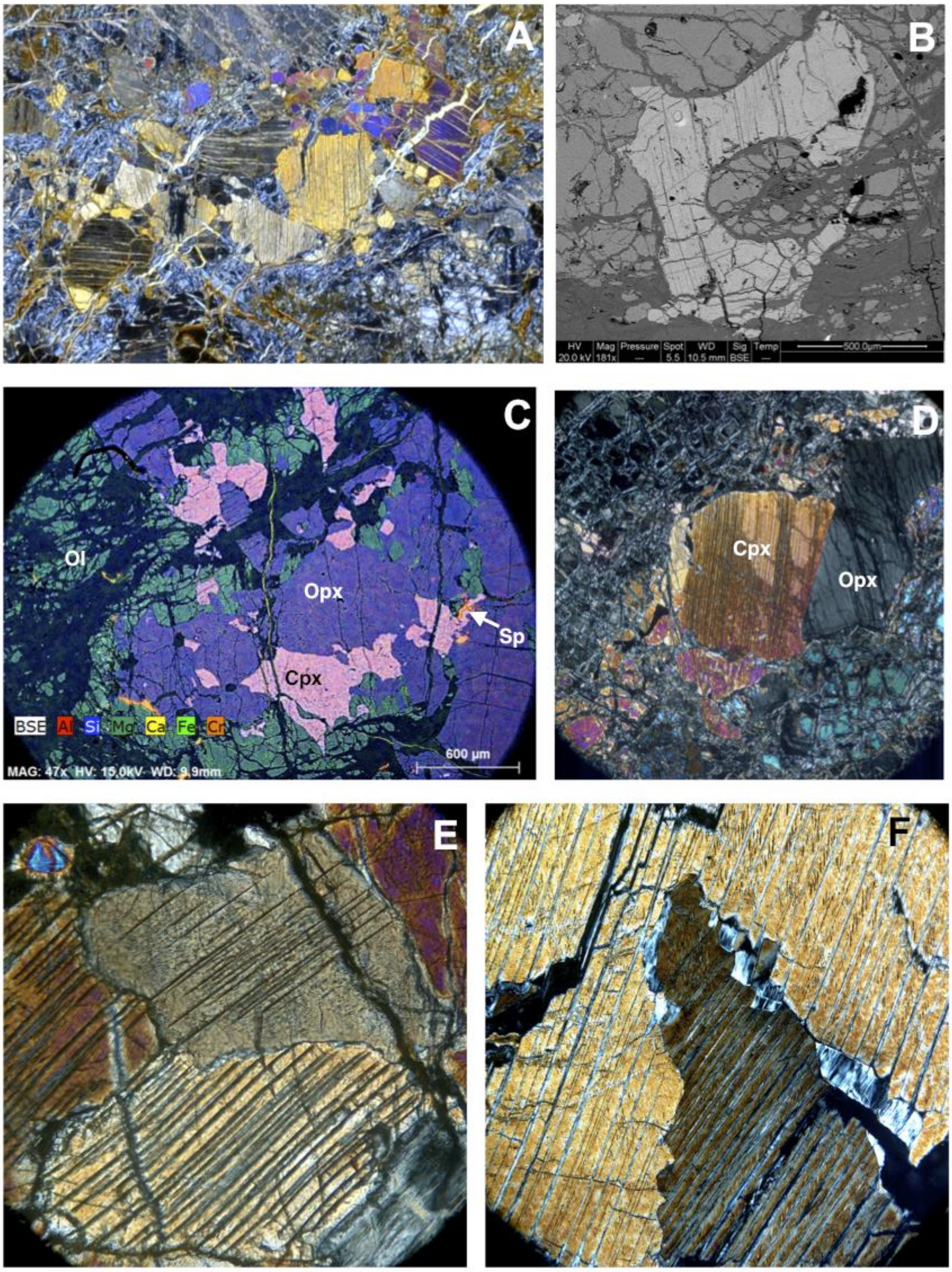
A
B
HV 20.0 kV
Mag 181x
Pressure ---
Spot 5.5
WD 10.5 mm
Sig BSE
Temp ---
500.0µm
C
Ol
Opx
Cpx
Sp
BSE Al Si Mg Ca Fe Cr
MAG: 47x HV: 15.0kV WD: 9.9mm
600 µm
D
Cpx
Opx
E
F

Figure 3

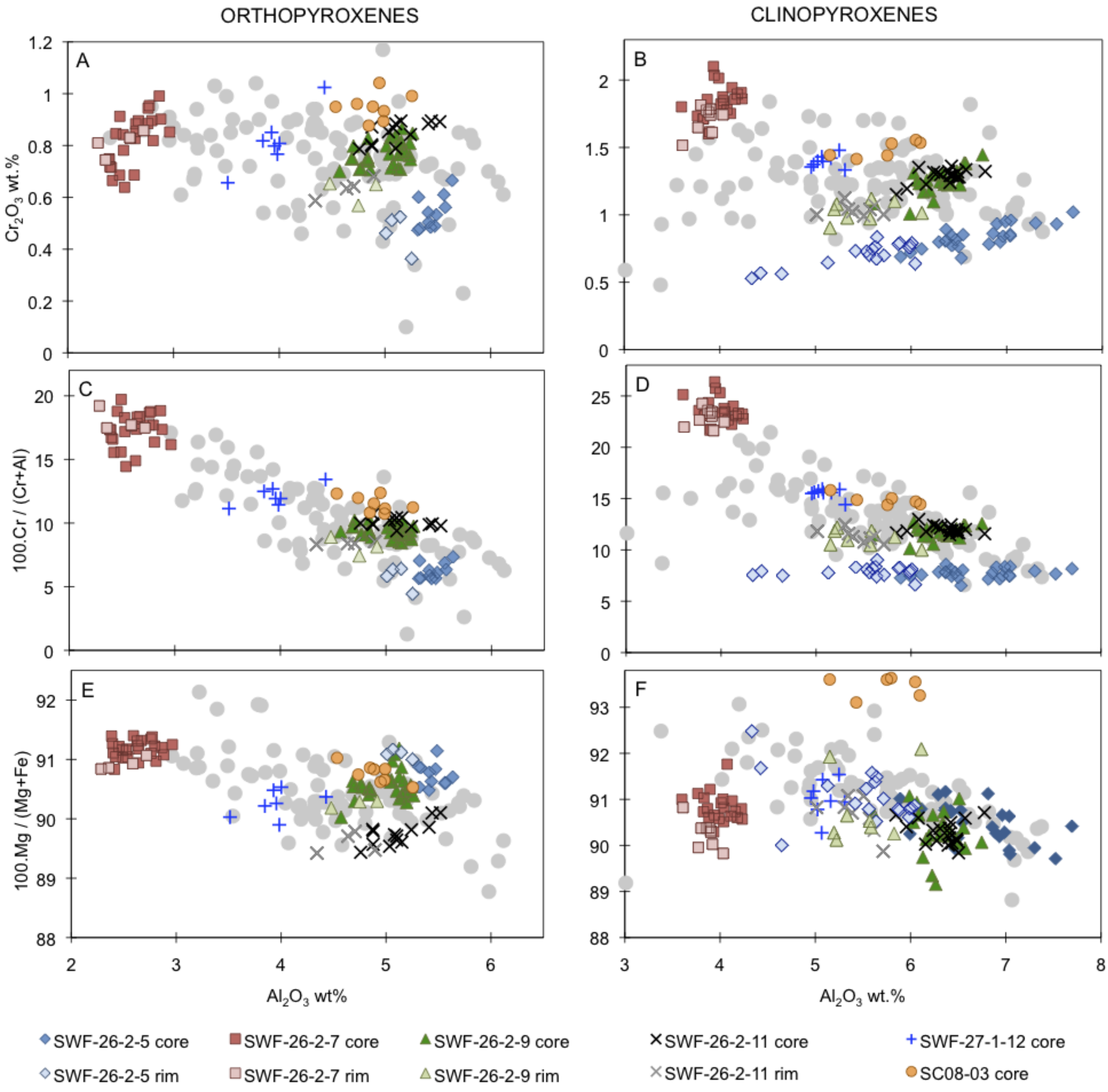
ORTHOPYROXENES
CLINOPYROXENES
A
B
C
D
E
F
Cr_2O_3 wt.%
100.Cr / (Cr+Al)
100.Mg / (Mg+Fe)
Al_2O_3 wt%
Al_2O_3 wt.%
0
0.2
0.4
0.6
0.8
1
1.2
0.5
1.5
2
5
10
15
20
25
88
89
90
91
92
93
2
3
4
5
6
7
8
SWF-26-2-5 core
SWF-26-2-5 rim
SWF-26-2-7 core
SWF-26-2-7 rim
SWF-26-2-9 core
SWF-26-2-9 rim
SWF-26-2-11 core
SWF-26-2-11 rim
SWF-27-1-12 core
SC08-03 core

Figure 4

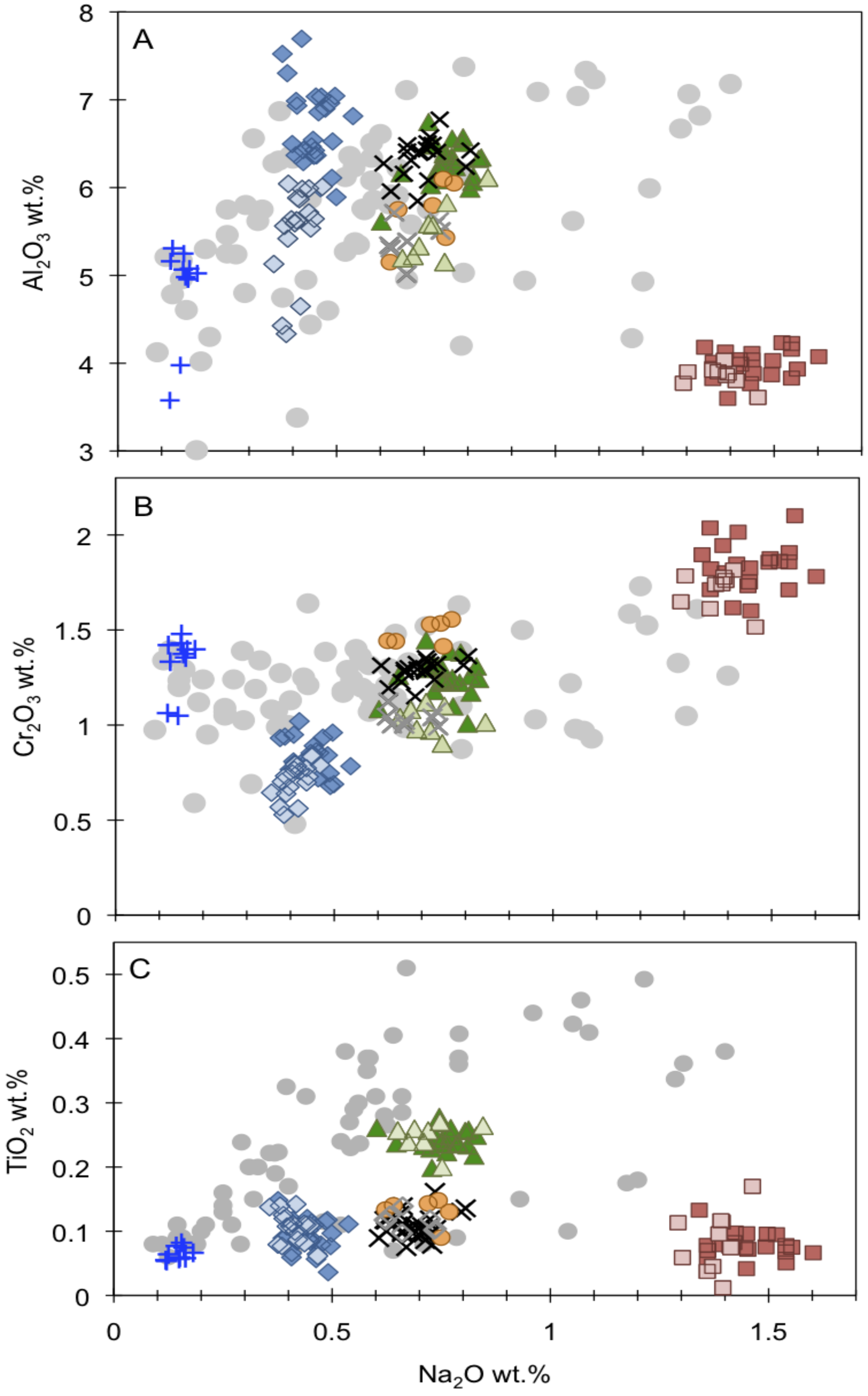
A
B
C
Al$_2$O$_3$ wt.%
Cr$_2$O$_3$ wt.%
TiO$_2$ wt.%
Na$_2$O wt.%
8
7
6
5
4
3
2
1.5
1
0.5
0
0.5
0.4
0.3
0.2
0.1
0
0
0.5
1
1.5

Figure 5

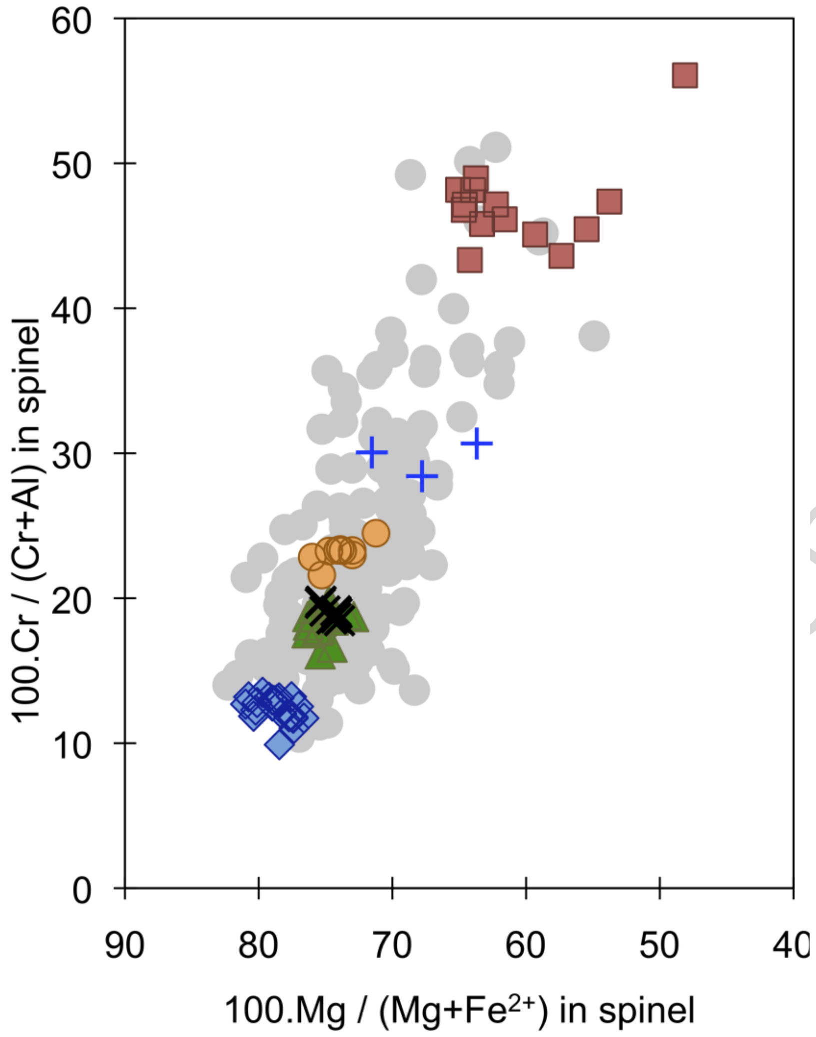
60
50
40
30
20
10
0
100.Cr / (Cr+Al) in spinel
90
80
70
60
50
40
100.Mg / (Mg+Fe^{2+}) in spinel

Figure 6

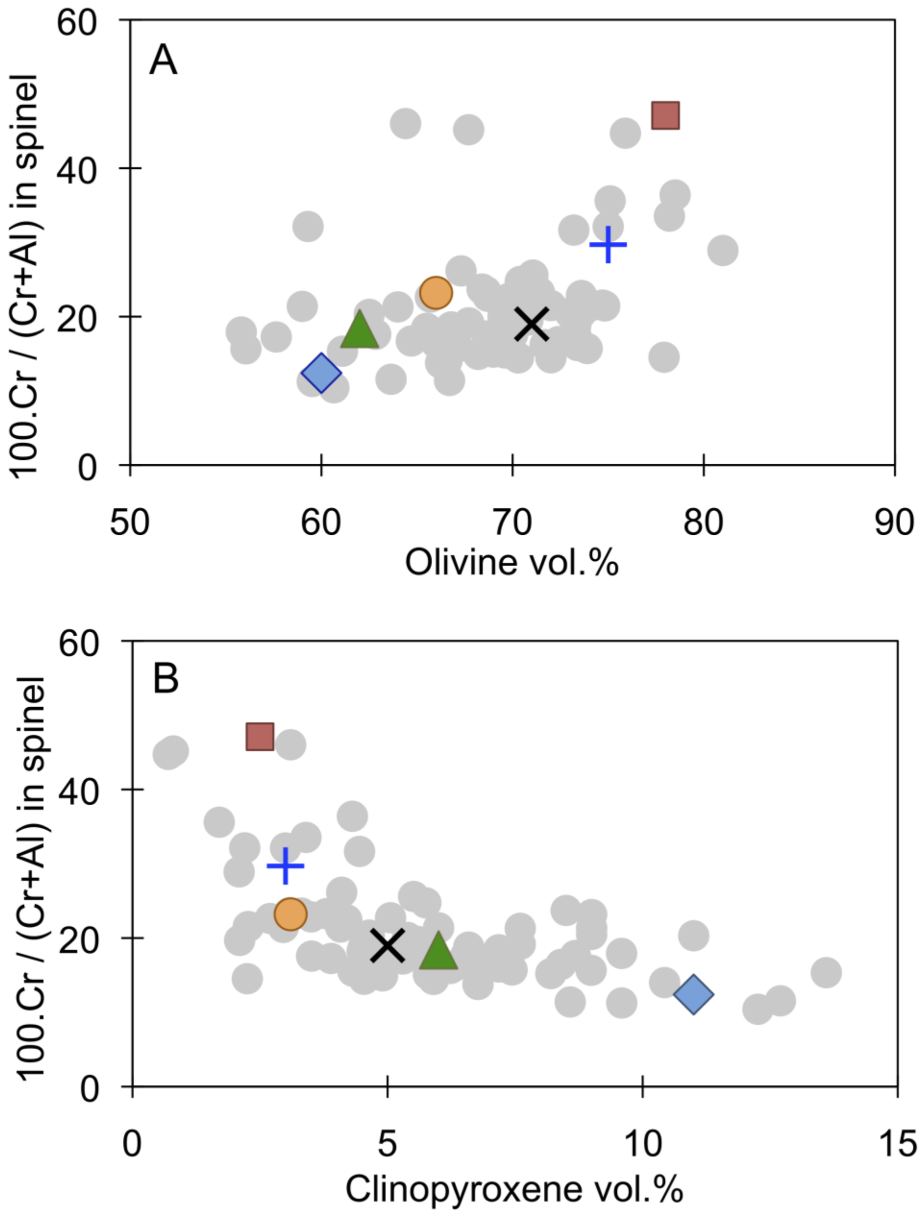
A
60
40
20
0
100.Cr / (Cr+Al) in spinel
50
60
70
80
90
Olivine vol.%
B
60
40
20
0
100.Cr / (Cr+Al) in spinel
0
5
10
15
Clinopyroxene vol.%

Figure 7

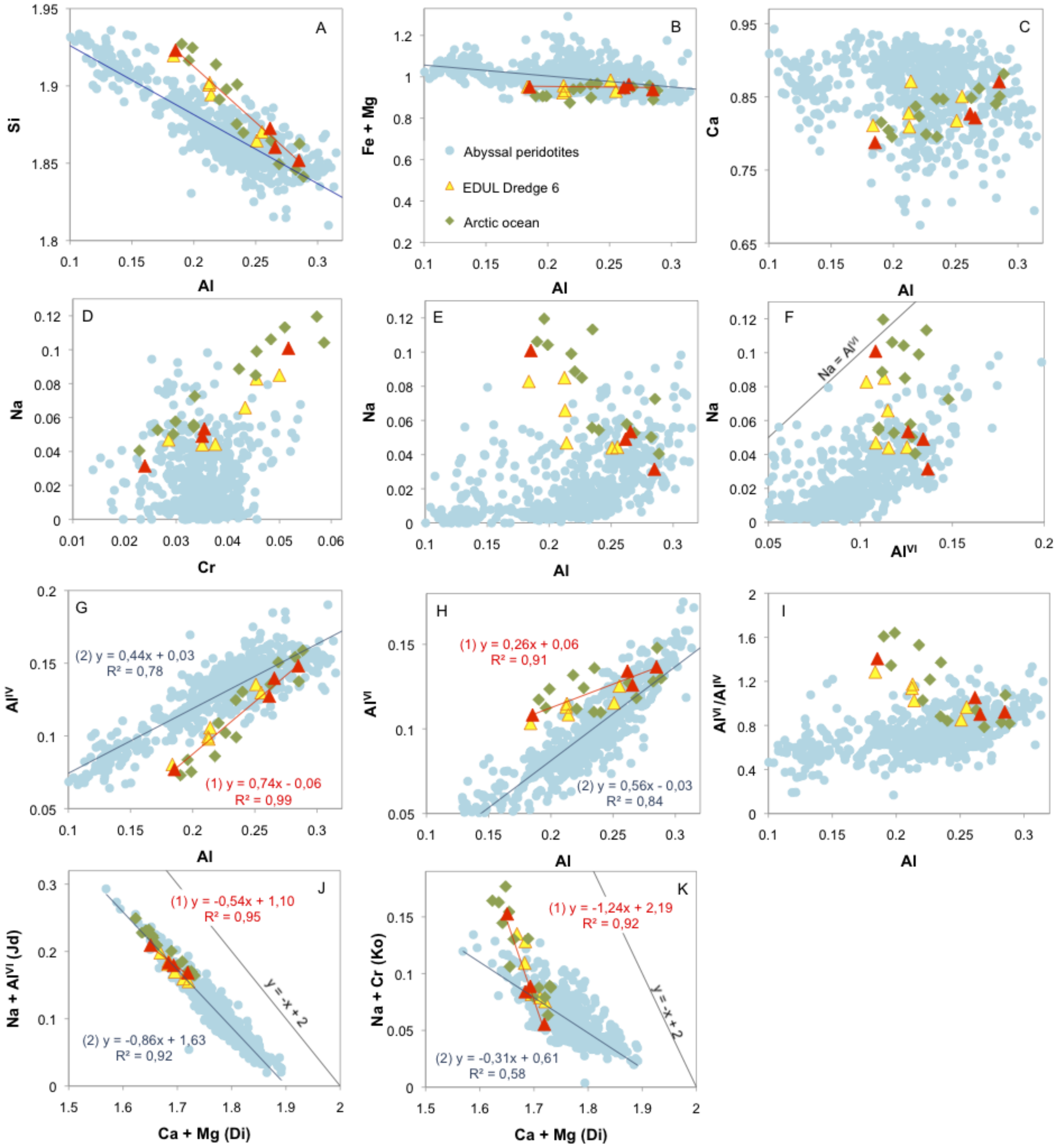
A
Si
1.95
1.9
1.85
1.8
0.1
0.15
0.2
0.25
0.3
Al
B
Fe + Mg
1.2
1
0.8
0.6
0.4
0.2
Abyssal peridotites
EDUL Dredge 6
Arctic ocean
Al
C
Ca
0.95
0.85
0.75
0.65
Al
D
Na
0.12
0.1
0.08
0.06
0.04
0.02
0
0.01
0.02
0.03
0.04
0.05
0.06
Cr
E
Na
Al
F
Na
Na = Al^{VI}
0.05
0.1
0.15
0.2
Al^{VI}
G
Al^{IV}
(2) y = 0,44x + 0,03
R² = 0,78
(1) y = 0,74x - 0,06
R² = 0,99
Al
H
Al^{VI}
(1) y = 0,26x + 0,06
R² = 0,91
(2) y = 0,56x - 0,03
R² = 0,84
Al
I
Al^{VI}/Al^{IV}
2
1.6
1.2
0.8
0.4
0
Al
J
Na + Al^{VI} (Jd)
(1) y = -0,54x + 1,10
R² = 0,95
(2) y = -0,86x + 1,63
R² = 0,92
y = -x + 2
0.3
0.2
0.1
0
1.5
1.6
1.7
1.8
1.9
2
Ca + Mg (Di)
K
Na + Cr (Ko)
(1) y = -1,24x + 2,19
R² = 0,92
(2) y = -0,31x + 0,61
R² = 0,58
y = -x + 2
0.15
0.1
0.05
0
Ca + Mg (Di)

Figure 8

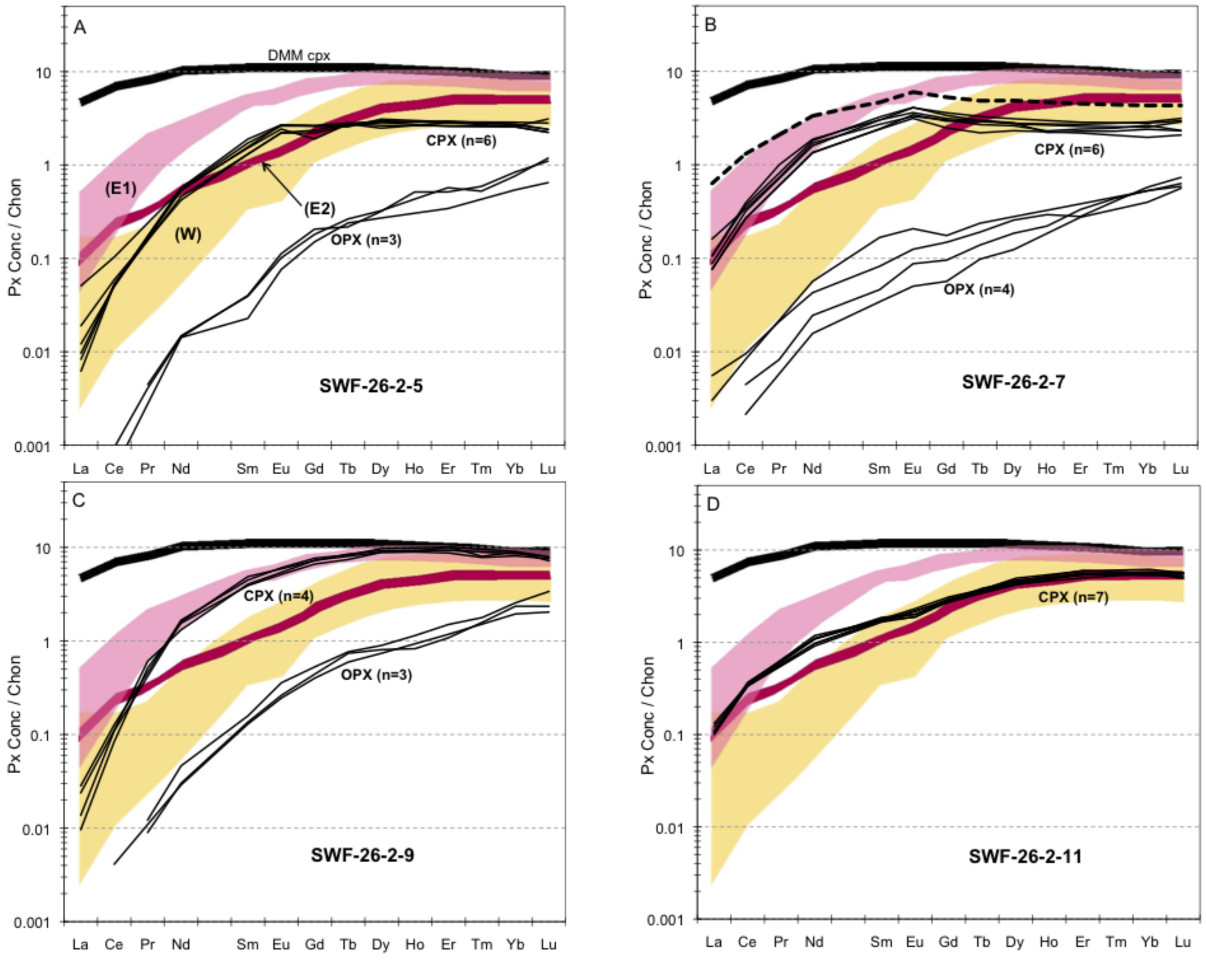
A
DMM cpx
(E1)
(W)
(E2)
CPX (n=6)
OPX (n=3)
SWF-26-2-5
B
CPX (n=6)
OPX (n=4)
SWF-26-2-7
C
CPX (n=4)
OPX (n=3)
SWF-26-2-9
D
CPX (n=7)
SWF-26-2-11
Px Conc / Chon
10
1
0.1
0.01
0.001
La Ce Pr Nd Sm Eu Gd Tb Dy Ho Er Tm Yb Lu

Figure 9

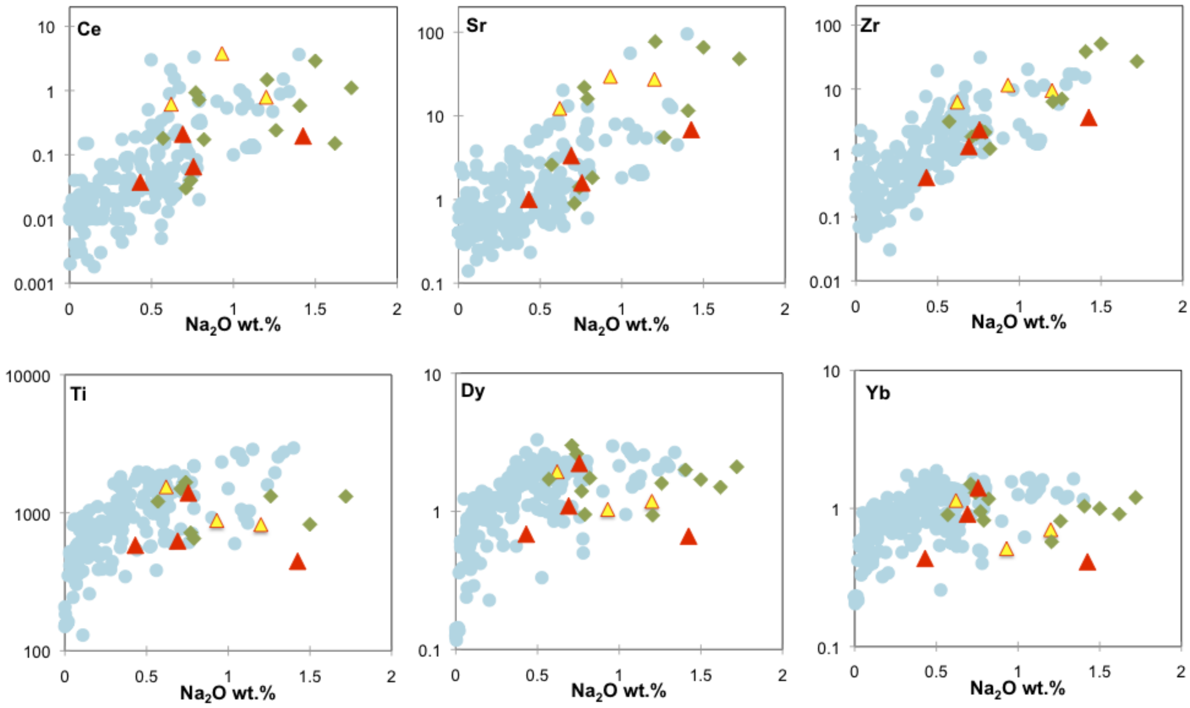
Ce
10
1
0.1
0.01
0.001
0
0.5
1
1.5
2
Na2O wt.%
Sr
100
10
1
0.1
Zr
100
10
1
0.1
0.01
Ti
10000
1000
100
Dy
10
1
0.1
Yb
10
1
0.1

Figure 10

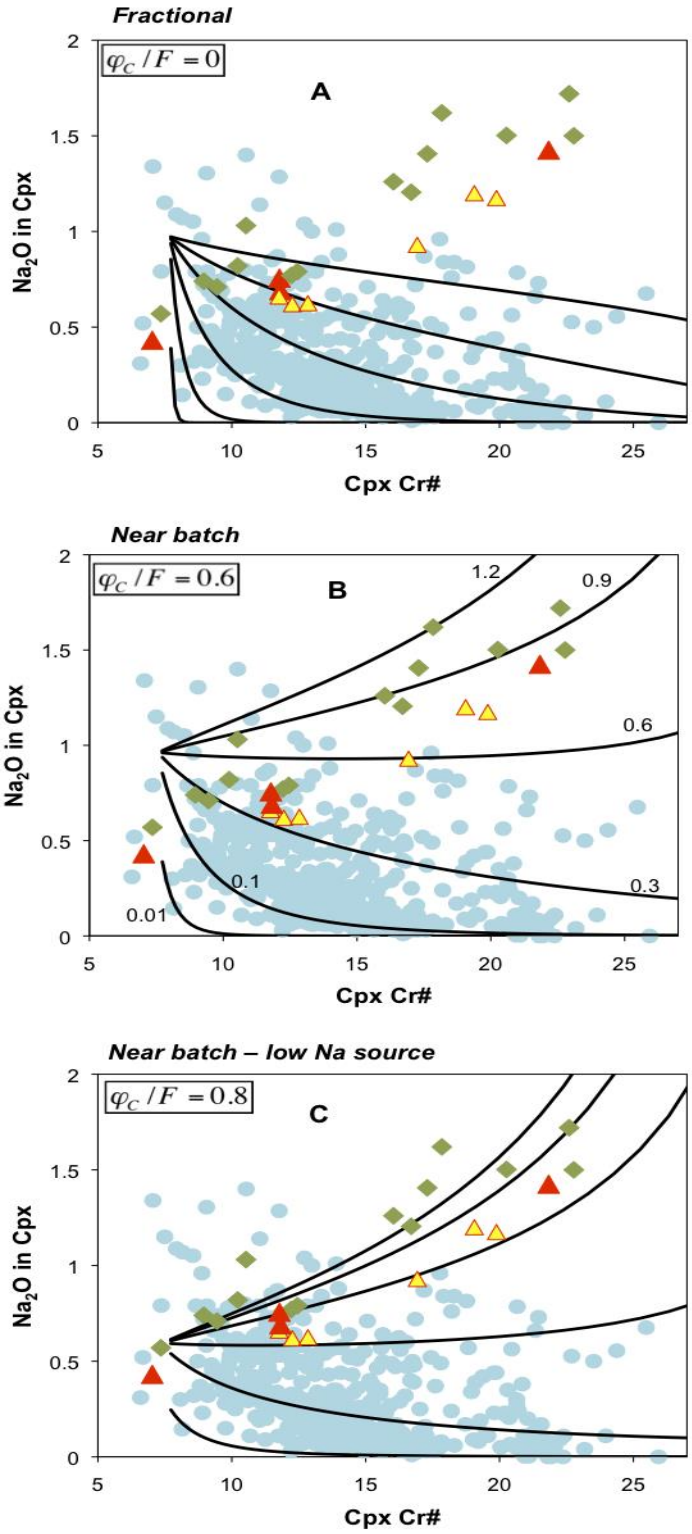
Fractional
$\varphi_C / F = 0$
A
Na$_2$O in Cpx
Cpx Cr#
Near batch
$\varphi_C / F = 0.6$
B
1.2
0.9
0.6
0.3
0.1
0.01
Near batch – low Na source
$\varphi_C / F = 0.8$
C
0
0.5
1
1.5
2
5
10
15
20
25

Figure 11

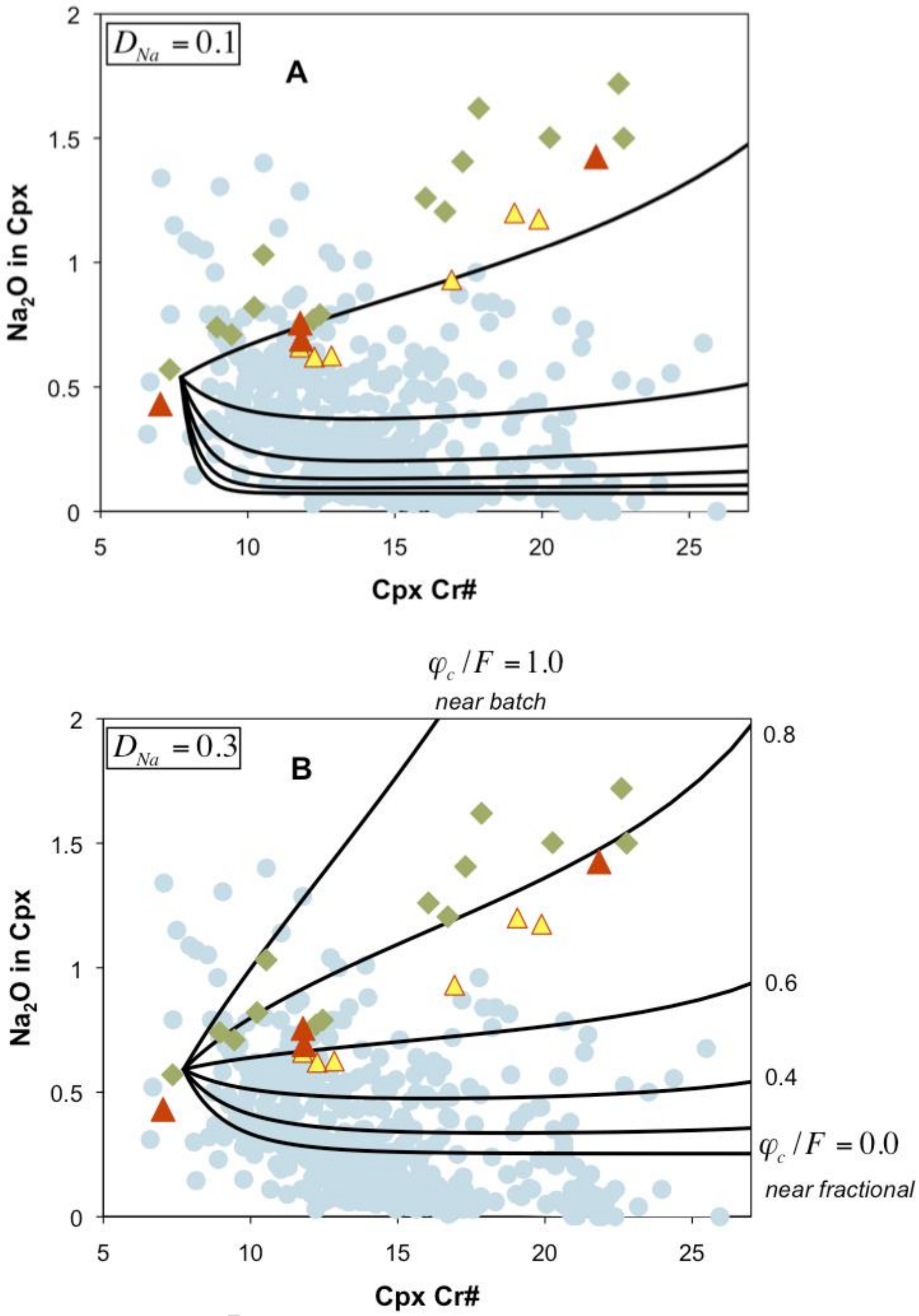
$D_{Na} = 0.1$
A
Na$_2$O in Cpx
2
1.5
1
0.5
0
5
10
15
20
25
Cpx Cr#
$\varphi_c / F = 1.0$
near batch
$D_{Na} = 0.3$
B
0.8
0.6
0.4
$\varphi_c / F = 0.0$
near fractional
Na$_2$O in Cpx
2
1.5
1
0.5
0
5
10
15
20
25
Cpx Cr#

Figure 12

Table 1
Reconstructed primary modal compositions

				Mode				
Sample	Lat (°S)	Long (°E)	Depth (m)	Olivine	Opx	Cpx	Spinel	Points
SWF-26-2-5	40.98	44.03	3170	60	26	11	3	8847
SWF-26-2-7	40.98	44.03	3170	78	19	2.5	0.5	5274
SWF-26-2-9	40.98	44.03	3170	62	31	6	1	6122
SWF-26-2-11	40.98	44.03	3170	71	23	5	1	4133
SWF-27-1-12	41.04	44.48	3070	75	22	3	0.5	1862
SC-08-03	39.50	45.51	na	66	31	2	1	1657

Point counts on 1 to 3 standard-sized thin sections, 0.5 mm spacing
na = not available

Table 2a
Major element composition of olivines in wt.%

Sample	# Grains	# Spots	SiO_2	FeO	MnO	NiO	MgO	CaO	Total	Fo
SWF-26-2-5	10	14	41.37	8.63	0.13	0.37	48.81	0.03	99.35	90.97
SWF-26-2-7	20	29	41.19	8.87	0.13	0.39	49.04	0.05	99.68	90.79
SWF-26-2-9	8	12	40.83	9.17	0.12	0.38	48.29	0.04	98.83	90.37
SWF-26-2-11	8	15	41.23	9.36	0.12	0.37	48.18	0.06	99.32	90.17

Table 2b
Major element composition of orthopyroxenes in wt.%

Sample	# Grains	# Spots	SiO_2	TiO_2	Al_2O_3	Cr_2O_3	FeO	MnO	NiO	MgO	CaO	Na_2O	Total	Cr#	Mg#
SWF-26-2-5	3	15	54.58	0.02	5.36	0.52	5.79	0.13	0.08	32.20	1.38	0.03	100.08	6.11	90.83
SWF-26-2-7	9	29	56.27	0.03	2.60	0.82	5.87	0.14	0.10	33.88	1.39	0.11	101.21	17.45	91.14
SWF-26-2-9	11	45	54.49	0.08	5.07	0.79	6.00	0.13	0.10	31.94	1.55	0.06	100.22	9.48	90.47
SWF-26-2-11	4	17	54.34	0.04	5.00	0.80	6.18	0.13	0.09	30.23	1.59	0.06	98.46	9.69	89.71
SWF-27-1-12	3	8	55.66	0.03	3.95	0.82	6.13	0.13	0.10	31.89	1.62	0.06	100.38	12.15	90.26
SC-08-03	1	8	54.54	0.04	4.90	0.95	5.69	0.11	0.10	31.37	1.93	0.05	99.68	11.51	90.76

Table 2c
Major element composition of clinopyroxenes in wt.%

Sample	# Grains	# Spots	SiO_2	TiO_2	Al_2O_3	Cr_2O_3	FeO	MnO	NiO	MgO	CaO	Na_2O	Total	Cr#	Mg#
SWF-26-2-5	13	43	51.31	0.10	6.20	0.78	2.92	0.09	0.05	16.00	22.66	0.43	100.54	7.80	90.72
SWF-26-2-5*	7	24	51.33	0.09	6.70	0.84	2.95	0.09	0.05	15.78	22.52	0.45	100.82	7.75	90.50
SWF-26-2-7	11	30	52.86	0.08	3.95	1.80	2.92	0.08	0.05	15.91	20.21	1.43	99.28	23.39	90.66
SWF-26-2-9	16	45	51.04	0.22	6.18	1.23	3.01	0.09	0.05	16.05	21.03	0.76	99.66	11.75	90.49
SWF-26-2-11	9	25	51.15	0.11	6.06	1.21	2.97	0.09	0.05	15.71	21.08	0.69	99.13	11.80	90.41
SWF-27-1-12	5	7	51.51	0.06	5.10	1.40	2.96	0.12	0.05	16.83	21.48	0.15	99.66	15.53	91.02
SC-08-03	5	6	51.50	0.13	5.71	1.49	1.93	0.04	0.06	15.48	22.47	0.71	99.52	14.88	93.46

* Core composition

Table 2d
Major element composition of spinels in wt.%

Sample	# Grains	# Spots	SiO_2	TiO_2	Al_2O_3	Cr_2O_3	Fe_2O_3	FeO	MnO	MgO	NiO	Total	Cr#	Mg#
SWF-26-2-5	10	22	0.06	0.02	54.61	11.47	2.77	9.58	0.10	19.80	0.37	98.77	12.35	78.67
SWF-26-2-7	8	14	0.08	0.06	27.67	36.65	4.78	15.36	0.22	13.24	0.14	98.17	47.09	60.53
SWF-26-2-9	10	18	0.04	0.06	49.46	16.66	2.21	10.87	0.11	18.35	0.31	98.00	18.43	75.05
SWF-26-2-11	2	8	0.04	0.03	48.76	17.10	2.19	10.96	0.12	18.06	0.31	97.58	19.04	74.61
SWF-26-2-12*	1	4	0.72	0.00	38.32	26.41	1.99	14.36	n.a.	15.46	0.20	97.46	31.61	65.74
SWF-27-1-12	3	3	0.01	0.03	41.41	26.10	1.19	13.53	0.15	15.89	0.12	98.41	29.72	67.67
SC-08-03	5	9	0.03	0.03	46.47	20.87	1.02	11.22	n.a.	17.80	0.25	97.70	23.16	73.88

*Harzburgite in which spinel is the only fresh mineral phase

Table 3
Trace element composition of pyroxenes in ppm

		SWF-26-2-5	SWF-26-2-5	SWF-26-2-7	SWF-26-2-7	SWF-26-2-9	SWF-26-2-9	SWF-26-2-11
		cpx	opx	cpx	opx	cpx	opx	cpx
Ba		0.06	0.06	0.07	0.03	0.11	0.002	0.30
	S.D.	0.08	0.07	0.07	0.03	0.12		0.21
Nb		0.11	0.01	0.23	0.01	0.16	0.01	0.17
	S.D.	0.04	0.00	0.11	0.01	0.10	0.01	0.02
Sr		1.01	0.71	6.86	0.30	1.58	0.20	3.34
	S.D.	0.19	1.04	1.23	0.22	0.51	0.21	1.06
Zr		0.41	0.09	3.59	0.56	2.30	0.65	1.27
	S.D.	0.10	0.05	0.32	0.31	0.28	0.31	0.05
Hf		0.06	0.01	0.10	0.02	0.21	0.05	n.a.
	S.D.	0.01	0.00	0.01	0.00	0.02	0.00	
Ti		581.9	278.0	445.6	265.5	1393.5	640.4	625.0
	S.D.	65.1	49.9	18.0	74.0	104.3	49.1	20.0
Y		4.18	0.55	3.47	0.40	13.09	1.77	7.85
	S.D.	0.24	0.05	0.40	0.08	0.73	0.24	0.38
La		0.004	0.018	0.024	0.001	0.004	b.d.	0.026
	S.D.	0.004	0.025	0.007	0.000	0.002		0.003
Ce		0.037	bd	0.196	0.004	0.065	0.002	0.210
	S.D.	0.012		0.030	0.002	0.011		0.007
Pr		0.025	bd	0.077	0.001	0.025	0.001	0.077
	S.D.	0.007		0.017	0.001	0.006	0.000	0.000
Nd		0.233	0.007	0.730	0.016	0.693	0.016	0.473
	S.D.	0.027	0.000	0.102	0.008	0.069	0.004	0.044
Sm		0.228	0.005	0.412	0.012	0.636	0.021	0.257
	S.D.	0.034	0.002	0.051	0.009	0.065	0.002	0.009
Eu		0.139	0.005	0.202	0.007	0.315	0.016	0.116
	S.D.	0.013	0.001	0.023	0.004	0.024	0.003	0.009
Gd		0.470	0.035	0.607	0.023	1.415	0.090	0.565
	S.D.	0.059	0.005	0.076	0.010	0.084	0.013	0.025
Tb		0.099	0.009	0.103	0.006	0.293	0.025	0.132
	S.D.	0.003	0.001	0.013	0.002	0.017	0.003	0.006
Dy		0.685	0.074	0.662	0.051	2.224	0.198	1.094
	S.D.	0.054	0.007	0.063	0.017	0.094	0.019	0.063
Ho		0.162	0.026	0.126	0.014	0.499	0.055	n.a.
	S.D.	0.025	0.003	0.004	0.003	0.004	0.012	
Er		0.444	0.076	0.397	0.050	1.519	0.199	0.881
	S.D.	0.023	0.019	0.040	0.008	0.106	0.035	0.055
Tm		0.058	0.014	0.057	0.010	0.058	0.041	0.057
	S.D.	0.007	0.001	0.003	0.001	0.004	0.003	0.000
Yb		0.435	0.116	0.411	0.082	1.409	0.371	0.911
	S.D.	0.020	0.025	0.053	0.012	0.069	0.050	0.049
Lu		0.062	0.024	0.064	0.015	0.186	0.063	0.132
	S.D.	0.008	0.007	0.010	0.002	0.008	0.017	0.007

Compositions average several grains of several textural types when variation is within analytical errors.
S.D. is the standard deviation, lacking if only one measure is above detection limit. Complete data set is given in Supplementary Table S1.
n.a. means not analyzed; b.d. means below detection limit.

Table 4

Cation numbers per formula unit and molecular components of clinopyroxenes of SWF-26-2-5 and SWF-26-2-7

SWF-26-2-5					SWF-26-2-7				
Cations per formula unit		Component	(1)	(2)	Cations per formula unit		Component	(1)	(2)
Si	1.850	Jd	0.031	0.008	Si	1.930	Jd	0.101	0.049
Ti	0.002	Ko	0	0.023	Ti	0.002	Ko	0	0.052
Al^{IV}	0.152	CrCaTs	0.024	0	Al^{IV}	0.070	CrCaTs	0.052	0
Al^{VI}	0.133	CaTs	0.102	0.125	Al^{VI}	0.107	CaTs	0	0.058
Cr	0.024	CaTiTs	0.002	0.002	Cr	0.052	CaTiTs	0.002	0.002
Fe	0.089	DiHd	0.742	0.742	Fe	0.089	DiHd	0.727	0.727
Mg	0.848	EnFs	0.097	0.097	Mg	0.862	EnFs	0.112	0.112
Ca	0.870	Sum	0.999	0.999	Ca	0.787	Sum	1.000	1.000
Na	0.031	Sum CaTs	0.128	0.128	Na	0.101	Sum CaTs	0.060	0.060
Total	4.000	Si residual	-0.017	-0.017	Total	4.000	Si residual	-0.008	-0.008

See text for the detail of calculations and the meaning of abbreviations

Highlights

1- The compositions of mantle-derived peridotites dredged at the Southwest Indian Ridge axis between Discovery and Indomed fracture zones span the whole compositional range of abyssal, residual spinel peridotites, even at a dredge scale.

2- Their clinopyroxenes are characterized by unusual compositions, marked by a large covariation in sodium and chromium in residual clinopyroxenes while aluminum decreases, leading to extreme enrichments in both elements in correletion with increasing refractory composition of the peridotite hosts.

3- Despite this odd behaviour, the microstructures and other geochemical features (such as, very low LREE/HREE ratios and Ti contents in pyroxenes and spinel) are typical of residual peridotites.

4- Numerical modeling suggests that the peridotite interacted with a sodium-rich melt during partial melting in the upwelling mantle.